Angiogenic switching in cerebral cavernous malformations driven by MAP3K3–PIK3CA synergy

Jian Ren,[1,2,3,†] Yeqing Ren,[1,2,3,†] An Tian,[1,2,3,†] Ziwei Cui,[1,2] Daochao Wang,[1,2] Hao Yu,[1,2] Chendan Jiang,[1,2] Jiaxing Yu,[1,2] Shikun Zhang,[1,2] Jing Chen,[1,2] Shuang Liang,[3] Yu Gu,[3] Yiqing Wang,[1,2] Jianfeng Lei,[4] Xiangjian Zheng,[5] Dong Xing,[6,7] Hongqi Zhang[1,2] and Tao Hong[1,2,3,8]

[†] **These authors contributed equally to this work.**

Abstract

Cerebral cavernous malformations are common vascular anomalies in the central nervous system that predispose individuals to seizures and hemorrhagic stroke. Familial forms are linked to germline loss-of-function mutations in *CCM1–3*, and sporadic lesions frequently harbor somatic gain-of-function mutations in *MAP3K3* and *PIK3CA*. However, the mechanisms by which these somatic mutations drive lesion development remain incompletely understood, and no medical therapies are currently available.

Here, we investigated the cooperative effects of *MAP3K3*$^{\mathrm{I441M}}$ and *PIK3CA*$^{\mathrm{H1047R}}$ mutations using transgenic neonatal and adult mouse model, supported by histology, micro-CT, bulk and single-cell RNA sequencing, and human cerebral cavernous malformations samples.

MAP3K3$^{\mathrm{I441M}}$ activated inflammatory and angiogenic transcriptional programs in brain endothelial cells, whereas *PIK3CA*$^{\mathrm{H1047R}}$ enhanced cell cycle and DNA replication pathways. Notably, *MAP3K3*$^{\mathrm{I441M}}$ and *PIK3CA*$^{\mathrm{H1047R}}$ double mutations synergistically amplified PI3K–AKT–mTOR signaling, inducing an "angiogenic switch" reminiscent of tumor neovascularization. This interaction promoted endothelial angiogenesis and lesion development in mouse brains. Transcriptomic analyses of human cerebral cavernous malformations confirmed enrichment of angiogenesis-related gene signatures in double mutations-related lesions. Treatment with the

PI3Kα-selective inhibitor alpelisib suppressed lesion formation and reversed pro-angiogenic signaling in both mouse models and patient-derived cerebral cavernous malformations organoids. These findings uncover a convergent mechanism involving MAPK and PI3K pathway activation in cerebral cavernous malformations pathogenesis and demonstrate that PI3Kα inhibition may offer a viable therapeutic strategy for a disease that currently lacks effective pharmacological treatment.

Author affiliations:

1 Department of Neurosurgery, Xuanwu Hospital, Capital Medical University, Beijing, 100053, China
2 Department of Neurosurgery, China International Neuroscience Institute (China-INI), Beijing, 100053, China
3 Laboratory for Clinical Medicine, Capital Medical University, Beijing, China
4 Medical Imaging laboratory of Core Facility Center, Capital Medical University; Beijing, 100069, China
5 Department of Pharmacology and Tianjin Key Laboratory of Inflammation Biology, School of Basic Medical Sciences, and Center for Cardiovascular Diseases, Tianjin Medical University, Tianjin, 300070, China
6 Biomedical Pioneering Innovation Center (BIOPIC), School of Life Sciences, Peking University, Beijing, 100871, China
7 Beijing Advanced Innovation Center for Genomics (ICG), Peking University, Beijing, 100871, China
8 Department of Neurosurgery, Xiongan Xuanwu Hospital, Xiong'an New Area, 071700, China

Correspondence to: Tao Hong
Department of Neurosurgery, Xuanwu Hospital, Capital Medical University, 45 Changchun St, Beijing, 100053, China
E-mail: hongtao.edu@gmail.com

Correspondence may also be addressed to: Hongqi Zhang

Department of Neurosurgery, Xuanwu Hospital, Capital Medical University, 45 Changchun St,
Beijing, 100053, China
E-mail: xwzhanghq@163.com

Running title: Angiogenic Switch in CCM
Keywords: vascular malformations; PI3K pathway activation; endothelial cell remodeling; targeted therapy; organoid disease models; somatic mutations

Introduction

Vascular malformations are congenital anomalies of blood vessel structure and function that range from benign to life-threatening.[1] Among these, cerebral cavernous malformations (CCMs) are characterized by clusters of dilated, irregular capillaries lacking normal intervening brain tissue, rendering them highly susceptible to hemorrhage.[2] CCMs are a leading cause of stroke and neurological deficits in young adults.[2, 3] Despite their clinical impact, there are no effective medical therapies. Surgical resection remains the primary therapeutic option but is often limited by lesion multiplicity, deep location, or surgical risk.[4]

Familial CCMs arise from loss-of-function (LOF) mutations in *KRIT1* (*CCM1*), *CCM2*, and *PDCD10* (*CCM3*).[5, 6] However, most cases are sporadic, and their molecular underpinnings are less well defined. Emerging evidence implicates activating mutations in the MAPK and PI3K pathways, particularly in *MAP3K3* and *PIK3CA*, in the pathogenesis of sporadic CCMs.[7-10] These mutations can occur independently or coexist in the same lesion, yet the mechanisms by which they interact to drive lesion development remain poorly defined.[9] *MAP3K3* encodes a serine/threonine kinase upstream in the MAPK cascade, while *PIK3CA* encodes the p110α catalytic subunit of PI3K, a key driver of PI3K–AKT–mTOR signaling.[11, 12] Prior studies showed that *PIK3CA* gain-of-function (GOF) mutations alone can induce developmental venous anomalies (DVAs) or early CCM-like lesions in neonatal brains.[13-15] Conversely, our findings demonstrate that overexpression of *MAP3K3* mutations can induce the formation of CCMs in mature brain tissue.[16] Additional factors, including microenvironmental secondary factors such as inflammation or microbial dysfunctions, may also contribute to the pathogenesis of CCMs.[17-20] In cancer, the “angiogenic switch” describes a transition from vascular quiescence to robust neovascularization, often driven by oncogenic mutations and hypoxia-induced VEGF signaling.[21, 22] Similar angiogenic hallmarks have been observed in CCMs, including VEGF overexpression and endothelial proliferation, yet the upstream regulators remain elusive.[23, 24]

Here, we demonstrate that *MAP3K3*$^{\mathrm{I441M}}$ synergizes with *PIK3CA*$^{\mathrm{H1047R}}$ to initiate a cancer-like angiogenic switch that drives CCM development. In brain endothelial cells, *MAP3K3*$^{\mathrm{I441M}}$ activates inflammatory and pro-angiogenic transcriptional programs, while *PIK3CA*$^{\mathrm{H1047R}}$ promotes cell cycle progression and DNA replication. Co-expression of these mutations amplifies PI3K–AKT–mTOR signaling, resulting in endothelial remodeling and lesion formation in adult mouse brains. This pathogenic mechanism was corroborated by transcriptomic and histological analyses of human CCM specimens, which exhibited angiogenic and inflammatory signatures consistent with MAP3K3 and PIK3CA activation. Notably, pharmacological inhibition of PI3Kα with alpelisib significantly suppressed lesion burden and reversed aberrant signaling in both preclinical mouse models and primary human CCM organoids, highlighting a promising therapeutic avenue. These findings elucidate a cooperative signaling mechanism underlying sporadic CCM progression and support PI3Kα inhibition as a viable strategy for treating this currently intractable cerebrovascular disease.

Materials and methods

Animals

R26–LSL–*Map3k3*$^{\mathrm{I441M}}$ animals were obtained from Shanghai Model Organisms Center. R26–LSL–*Pik3ca*$^{\mathrm{H1047R}}$ animals were obtained from the Jackson Laboratories (JAX catalogue number 016977). *Cdh5* (PAC)–CreERT2 animals were obtained from Cyagen Biosciences (catalogue number S-CKO-01668). *Slco1c1*(BAC)–CreERT2 animals were obtained from Shanghai Model Organisms Center. Ai14 Cre reporter animals were obtained from the Jackson Laboratories (JAX catalogue number 007914). Littermate controls were used for neonatal experiments unless otherwise indicated. Breeding pairs between two and eight months of age were used to generate neonatal CCM mouse models of the indicated genotypes. For all neonatal CCM experiments using the following models: *Cdh5* (PAC)–CreERT2; *Map3k3*$^{\mathrm{I441M}}$ (*Map3k3*$^{\mathrm{iECGOF}}$), *Cdh5* (PAC)–CreERT2; *Pik3ca*$^{\mathrm{H1047R}}$ (*Pik3ca*$^{\mathrm{iECGOF}}$), *Cdh5* (PAC)–CreERT2; *Map3k3*$^{\mathrm{I441M}}$; *Pik3ca*$^{\mathrm{H1047R}}$ (*Map3k3*$^{\mathrm{iECGOF}}$; *Pik3ca*$^{\mathrm{iECGOF}}$) and *Slco1c1*(BAC)–CreERT2; *Pik3ca*$^{\mathrm{H1047R}}$ (*Pik3ca*$^{\mathrm{iBECGOF}}$), postnatal day 1 (P1) pups were injected intragastrically with 40 μg of 4-hydroxytamoxifen (4-OHT, Sigma Aldrich) dissolved in 10% ethanol/corn oil vehicle (total volume of 50 µl per injection), using a 30-gauge needle. The 4-OHT solution was freshly prepared for every injection. The P1 time point was defined by checking experimental breeding pairs every evening for new litters. On the following morning (P1), pups were injected with 4-OHT in a blinded fashion without prior knowledge of their genotypes. Pups were then harvested at specified time points. Equal numbers of male and female animals were used in all experiments. Mice brains were imaged under a stereomicroscope. All animal experiments were performed in compliance with animal procedure protocols approved by Animal Experiments and Experimental Animal Welfare Committee of Capital Medical University.

Mice brain endothelial cells isolation

Mouse brains (excluding olfactory bulbs) were harvested after Avertin anesthesia and PBS perfusion. Tissue was digested in DMEM containing 1 mg/mL collagenase/dispase and 0.02 mg/mL DNase I at 37°C for 20 min with gentle shaking, then passed through a 70 µm strainer. Cells were centrifuged, resuspended, and incubated with anti-CD45 microbeads (Miltenyi) for 30 min at 4°C, followed by negative selection using MACS MS columns. The flow-through was then incubated with anti-CD31 microbeads for 30 min at 4°C and positively selected with MACS MS columns. $CD31^+$ endothelial cells were eluted, centrifuged, and processed for bulk RNA sequencing.

Histology, immunohistochemistry and immunofluorescence

For hematoxylin and eosin (H&E) staining, mouse brains were fixed in 4% paraformaldehyde (PFA) overnight, dehydrated in ethanol, embedded in paraffin, and sectioned at 5 µm. Sections were dewaxed, rehydrated, and stained with H&E using standard procedures. For Prussian blue DAB staining, paraffin sections were deparaffinized, rehydrated, and incubated in freshly prepared 2% potassium ferrocyanide and 2% hydrochloric acid (1:1) for 30 min at room temperature. After washing, sections were developed with DAB for 5–10 min, counterstained with hematoxylin, differentiated in acid alcohol, blued in ammonia water, dehydrated, and mounted. Iron deposits appeared brown, and nuclei blue under light microscopy. For immunofluorescence, mouse brains were fixed in 4% PFA overnight, cryoprotected in 30% sucrose, embedded in OCT, and sectioned at 16 µm. Primary antibodies included rat anti-PECAM (Dianova, DIA-310), rabbit anti-VEGFA (Proteintech, 19003-1-AP), and rabbit anti-phospho-S6 (CST, 4858S). Alexa Fluor-conjugated secondary antibodies (1:400, Invitrogen) were applied, followed by DAPI counterstaining. Images were acquired using Pannoramic Scan (3D HISTECH) and Zeiss LSM 880 confocal microscopes, and processed with ImageJ. All human studies were approved by the Ethics Committee of Xuanwu Hospital, Capital Medical University (approval no. 2019-044), in accordance with the Declaration of Helsinki. Written informed consent was obtained. Surgical specimens were fixed in 10% buffered formalin and paraffin-embedded. Primary antibodies included goat anti-PECAM (R&D, AF3628), rabbit anti-phospho-S6 (CST, 4858S), and rabbit anti-VEGFA (Proteintech, 19003-1-AP).

X-ray micro-CT based quantification of CCM

To quantify the volume of lesions via micro-computed tomography (micro-CT) in all experiments, harvested brains were preserved in 4% formaldehyde solution until further processing. The fixed samples were then immersion-stained with non-destructive iodine contrast. Images were obtained using a SkyScan1276 micro-CT scanner at Capital Medical University. Three-dimensional volume rendering and volume quantification were performed using Avizo 3D, following established protocol.[25, 26] Tissue preparation, imaging, and post-processing were performed independently by different researchers in a blinded manner.

MRI evaluation

MRI was performed using a Bruker 7.0T scanner (Pharmascan 70/16; Bruker, Germany) equipped with a 23 mm surface coil and a 12 cm self-shielded gradient system. Image acquisition was controlled via Paravision 5.1 software on a Linux workstation running Topspin 2.0. Mice were anesthetized with 5% isoflurane in 95% O_2 for induction and maintained with 2% isoflurane in 98% O_2 during scanning. Respiratory rate was continuously monitored using a physiological monitoring system. T2-weighted images were acquired using the RARE (rapid acquisition with relaxation enhancement) sequence with the following parameters: repetition time (TR) = 3500 ms, echo time (TE) = 33 ms, RARE factor = 4, field of view (FOV) = 21 × 21 mm, matrix = 256 × 256, and slice thickness = 0.5 mm.

Single-cell RNA sequencing and data analysis

Raw reads were processed using Cell Ranger (v8.0.0 for mouse, v6.1.2 for human) with respective reference genomes (mm10-2020-A and GRCh38-2020-A). Filtered gene expression matrices were analyzed in R using Seurat (v5.3.0 for mouse; v4.3.0 for human). Low-quality cells (nFeatures <300 or high mitochondrial content) were excluded. Data were normalized with SCTransform, followed by principal component analysis and batch correction using Harmony. Clustering and UMAP visualization were performed following standard Seurat workflows. Marker genes were identified using FindAllMarkers (only.pos=TRUE, min.pct=0.25, logfc.threshold=0.75), and major cell types were annotated based on canonical markers. Differentially expressed genes (DEGs) were defined by average logFC >0.25 (mouse) or >0.75 (human) and expression in >10–25% of cells. Gene Ontology enrichment analyses were performed using clusterProfiler (v4.10–4.14).

Cell culture and lentiviral infection

Human umbilical vein endothelial cells (HUVECs) were purchased from ScienCell and maintained in endothelial cell medium (ECM, ScienCell, 1001) containing 10% fetal bovine serum, 1% ECGS, 1% P/S solution at 37°C in 5% CO_2. Passages 3-7 of cells were used for all cell experiments. Lentiviruses encoding human *MAP3K3*^{I441M} mutations and human *PIK3CA*^{H1047R} mutations were obtained from OBiO Technology (Shanghai, China). HUVECs were plated in 6-well dishes at 70% confluence and were infected with lentivirus. 48 hours after lentivirus infection, HUVECs were harvested for subsequent Bulk RNA Sequence, Q-PCR and Western blot analysis.

Q-PCR

The total RNA was extracted using TRIzol Reagent (Invitrogen, 15596018), and complementary DNA (cDNA) was synthesized using ReverTra Ace® qPCR RT Master Mix (TOYOBO, FSQ-301). Q-PCR was performed with SYBR GREEN Realtime PCR Master Mix (TOYOBO, QPK-201). The following primers were used in this study:

GAPDH forward: 5’-GCTGTTGTCATACTTCTC-3’

GAPDH reverse: 5’-AAAGGGTCATCATCTCTG-3’

MAP3K3 forward: 5’-ACCAGCATCAACAGTGAGGG-3’

MAP3K3 reverse: 5’-TGACCTGTCCAAGGATTGGC-3’

PIK3CA forward: 5’-CCACGACCATCATCAGGTGAA-3’

PIK3CA reverse: 5’-CCTCACGGAGGCATTCTAAAGT-3’

VEGFA forward: 5’-AGGGCAGAATCATCACGAAGT-3’

VEGFA reverse: 5’-AGGGTCTCGATTGGATGGCA-3’

VEGFC forward: 5’-GAGGAGCAGTTACGGTCTGTG-3’

VEGFC reverse: 5’-TCCTTTCCTTAGCTGACACTTGT-3’

Western blot

Protein samples were subjected to SDS-PAGE gels, transferred to polyvinylidene fluoride (PVDF) membranes, and blocked with 5% fat-free milk. The membranes were incubated with primary antibodies against the target proteins at 4℃ overnight. The primary antibodies used were VEGFA (Proteintech, 19003-1-AP) and GAPDH (CST, 2118). The membranes were then washed with TBST to remove unbound primary antibodies. Secondary antibodies conjugated to horseradish peroxidase (HRP) were applied to the membranes and incubated for 1 hour at room temperature. The antigen-antibody complexes were visualized using enhanced chemiluminescence (ECL) supersensitive luminescent substrate according to the manufacturer's instructions. The membranes were exposed to chemiluminescent imaging film. The intensity of the protein bands was quantified using ImageJ software (National Institutes of Health).

RNA extraction, library preparation, sequencing, and analysis

Total RNA was extracted using Trizol and quality-checked (RIN >7.0, 28S:18S >1.8). Poly(A) mRNA (1 µg) was enriched, fragmented (~200 bp), reverse-transcribed, and converted to double-stranded cDNA, followed by end repair, A-tailing, adapter ligation, and PCR amplification. Libraries were quantified, validated by RT-qPCR, and sequenced as 150 bp paired-end reads on Illumina NovaSeq. Reads were quality-filtered, aligned to the reference genome (HISAT2), and quantified (StringTie). Differentially expressed genes (|log2FC| ≥1, p ≤0.05, FDR-corrected) were identified using DESeq and annotated via ENSEMBL, NCBI, UniProt, GO, and KEGG.

Adeno-associated virus injection

We obtained AAV-BR1-*MAP3K3*^{I441M}-EGFP-WPRE, AAV-BR1-*MAP3K3*^{WT}-EGFP-WPRE, AAV-BR1-VEGFA-WPRE, and AAV-BR1-EGFP-WPRE (as control) from PackGene Biotech, Guangzhou, China. Mice were injected with Adeno-associated virus 1×10^{11} genome copies per mouse through the orbital veins.

Alpelisib treatment

Map3k3^{iECGOF}; *Pik3ca*^{iECGOF} neonatal mice were treated with the p110α inhibitor alpelisib (MCE, HY-15244) at a dose of 50 mg/kg. The vehicle solution consisted of PBS containing 1% sodium carboxymethyl cellulose (MCE, HY-Y0703) and 0.5% Tween 80 (MCE, HY-Y1891). Alpelisib was dissolved in vehicle and administered intragastrically to mice at P7, P9, and P11 (last dose ~24 h before sacrifice) following 4-OHT induction at P5. For patient-derived CCM organoids, primary tissues were cultured in BBB medium for 7 days to form organoids, then treated with 50 μM alpelisib for another 7 days before collection for frozen sectioning and immunofluorescence.

Primary human CCM organoids culture

Primary human CCM organoids were generated with reference to previously described protocols with minor changes.[27] Freshly resected CCM tissue from one patient was placed in Hibernate medium on ice and transported to the lab. Samples were dissected under a stereo microscope, minced into ~0.5 mm fragments, and incubated in RBC lysis buffer for 10 min at room temperature, followed by two washes with H+GPSA medium. Tissue fragments were cultured individually in ultra-low attachment 6-well plates with BBB medium on a low-speed shaker at 37°C, 5% CO_2, and the medium was refreshed every three days. After 7 days, organoids reached morphological stability for pharmacologic studies.

Human CCM organoid genotyping

DNA extracted from the same lesion used for primary human CCM organoid culture was subjected to WES at 300× mean coverage. Libraries were sequenced on an Illumina platform (2 × 150-bp paired-end reads). Base-calling and demultiplexing was carried out using bcl2fastq v2.16.0.10 (Illumina, Inc.). Adaptor nucleotides and low-quality base cells were removed by Trimmomatics. Paired-end sequencing reads were aligned to the human reference genome hg19 (Genome Reference Consortium Human Reference 37, GRCh37) using Burrows-Wheeler Aligner v0.7.12 (BWA-MEM). Samtools v1.6 was used to sort and index the aligned bam file. The bam file was further processed for PCR-duplicate removal by Picard v1.119 (https://broadinstitute.github.io/picard/) and for base recalibration and indel realignment by the Genome Analysis Toolkit v3.6 (GATK). MuTect somatic mode with default parameters was used for single nucleotide variant (SNV) identification. Small insertions and deletions (indels) were detected using Scalpel. Identified SNVs and indels were annotated with ANNOVAR and visually inspected in the Integrative Genomics Viewer (IGV, https://igv.org/).

Statistics

The data in this study are expressed as the mean ± SD as noted in individual figure legends. Statistical analyses were performed using GraphPad PRISM software, version 9.0. The unpaired Student's two-tailed t-test, or one-way ANOVA followed by Tukey's multiple comparisons were used to assess the differences. Differences were considered statistically significant when $P < 0.05$.

Results

MAP3K3 GOF synergizes with PIK3CA GOF in mice

As *PIK3CA* mutations and *MAP3K3* mutations were identified coexisting in the same endothelial cells in CCM patients,[9] we hypothesized that the MAP3K3 GOF synergizes with PIK3CA GOF to promote CCM development. To investigate this synergistic effect *in vivo*, we used the *Cdh5* (PAC)–CreERT2 (Supplementary Fig. 1) to specifically drive expression of the *Map3k3*$^{\mathrm{I441M}}$ mutation (using a R26–LSL–*Map3k3*$^{\mathrm{I441M}}$ allele, generating i*Map3k3*$^{\mathrm{I441M}}$) and *Pik3ca*$^{\mathrm{H1047R}}$

mutation (using a R26–LSL–*Pik3ca*$^{\mathrm{H1047R}}$ allele, generating i*Pik3ca*$^{\mathrm{H1047R}}$) in endothelial cells. Following administration of 4–OHT at postnatal day 1 (P1), we analyzed the phenotypes of *Cdh5* (PAC)–CreERT2; *Map3k3*$^{\mathrm{I441M}}$ (*Map3k3*$^{\mathrm{iECGOF}}$), *Cdh5* (PAC)–CreERT2; *Pik3ca*$^{\mathrm{H1047R}}$ (*Pik3ca*$^{\mathrm{iECGOF}}$) and *Map3k3*$^{\mathrm{iECGOF}}$; *Pik3ca*$^{\mathrm{iECGOF}}$ littermates at P6 (Fig. 1A and B). Visual and micro-CT analysis demonstrated a significant synergistic impact of MAP3K3 GOF and PIK3CA GOF on lesion development in mice harboring *Map3k3*$^{\mathrm{I441M}}$ and *Pik3ca*$^{\mathrm{H1047R}}$ double mutations (Fig. 1C and D). H&E staining of brain section revealed that *Map3k3*$^{\mathrm{iECGOF}}$ mice developed scattered small vascular lesions in both hindbrain and forebrain, *Pik3ca*$^{\mathrm{iECGOF}}$ mice developed small vascular lesions predominantly in hindbrain, while *Map3k3*$^{\mathrm{iECGOF}}$; *Pik3ca*$^{\mathrm{iECGOF}}$ mice developed multiple small vascular lesions throughout the hindbrain and forebrain (Fig. 1E). Hemosiderin deposition is observed surrounding the dilated vascular sinusoids within the lesions, as revealed by Prussian blue staining, closely resembling that seen in human CCMs (Supplementary Fig. 2A). Immunostaining showed that the lining cells of the lesions expressed endothelial marker CD31, but not the lymphatic marker PROX1, effectively excluding lymphatic malformations (Supplementary Fig. 3). Previous mechanistic studies have shown that in CCMs phosphorylation of S6 ribosomal protein (P-S6) is elevated subsequent to PIK3CA GOF.[8] Consistent with prior studies, immunofluorescence staining on neonatal brain sections exhibited higher levels of P-S6 in endothelial cells lining vascular lesions in *Map3k3*$^{\mathrm{iECGOF}}$; *Pik3ca*$^{\mathrm{iECGOF}}$ mice compared to that in other groups (Fig. 1F and G). To ascertain the clinical relevance, we performed P-S6 immunofluorescence staining on surgical specimen sections from CCM patients with diverse mutations. The results showed that endothelial cells of lesions harboring *MAP3K3* and *PIK3CA* double mutations exhibited higher expression of P-S6 (Fig. 1H and I). These findings confirmed that MAP3K3 GOF synergizes with PIK3CA GOF and augmented the formation of CCMs.

To elucidate the cellular mechanisms by which *MAP3K3* and *PIK3CA* GOF mutations drive CCM formation, we performed single-cell RNA sequencing (scRNA-seq) on cerebellar tissues from *Map3k3*$^{\mathrm{iECGOF}}$; *Pik3ca*$^{\mathrm{iECGOF}}$ double-mutant mice and wild-type littermate controls. Mice were administered 4-OHT at P5 and harvested at P12 (Fig. 2A). Brains from double-mutant mice displayed visible lesions compared with controls (Fig. 2B). We constructed a scRNA-seq dataset comprising 53,164 high-quality single cells from four cerebellar samples—two double-mutant lesions and two control tissues—using the 10× Genomics platform (Fig. 2C–E). Unsupervised clustering and marker-based annotation identified eleven distinct cell populations, including neurons, neuron precursors, oligodendrocytes, neural stem cells, microglia, endothelial cells, oligodendrocyte precursor cells (OPCs), astrocytes, ependymal cells, pericytes, and fibroblasts (Fig. 2F–H). To further dissect the vascular compartment affected by *Map3k3* and *Pik3ca* GOF mutations, we re-clustered ECs and mural cells (pericytes and fibroblasts) from the combined single-cell dataset. This focused analysis yielded five major vascular subclusters, including three EC subtypes, one pericyte cluster, and one fibroblast cluster (Fig. 2J). Quantitatively, ECs accounted for 75.9% of total vascular cells (EC and mural cells) in the $Map3k3^{\mathrm{iECGOF}}$; $Pik3ca^{\mathrm{iECGOF}}$ double-mutant lesions, compared with 77.8% in wild-type controls (Fig. 2L). Gene Ontology (GO) analysis of endothelial subcluster 1 from mutant lesions revealed significant enrichment in biological processes related to angiogenesis regulation, vascular development, collagen metabolism, and macrophage migration (Fig. 2M). In contrast, pericytes from double-mutant samples showed upregulation of genes associated with endothelial differentiation, adhesion, and extracellular matrix organization (Fig. 2N). These findings suggest that *MAP3K3* and *PIK3CA* GOF mutations cooperatively alter endothelial–mural cell communication, promoting an activated, angiogenic vascular state that contributes to CCM lesion initiation and expansion.

MAP3K3 GOF activates pro-angiogenic pathways

To determine whether these mechanisms are conserved in human CCMs, we analyzed single-cell RNA-sequencing data from surgically resected human lesions using a previously published dataset.[28] This study included transcriptomic profiles from 12 samples: 3 controls and 9 CCM lesions categorized into the following mutation groups: 2 with *MAP3K3* mutations, 4 with *PIK3CA* mutations, 2 with *MAP3K3* and *PIK3CA* double mutations, and 1 with germline *KRIT1* mutations (K654Sfs*21) (Fig. 3A). The samples were sequenced using the 10x Genomics Chromium v2 platform, yielding data from 102,077 cells with 24,856 detected features. After stringent filtering, 73,434 cells were retained, comprising 21,085 normal cells and 52,349 cells from CCM lesions. The distribution of lesion cells was as follows: 11,013 from *MAP3K3* mutants, 21,118 from *PIK3CA* mutants, 14,091 from double mutants, and 6,127 from the germline *KRIT1* mutant group (Fig. 3B). Cell type annotation using the CellMarker 2.0 database identified nine major cell types: astrocytes, B cells, endothelial cells, macrophages, microglial cells, mural cells, neurons, oligodendrocytes, and T cells (Fig. 3C-E and Supplementary Fig. 4A). Given the central role of endothelial cells in CCM pathogenesis and their altered transcriptomic profiles across mutation groups, we focused further analysis on endothelial cell clusters from control and CCM samples with different genotypes. In total, 8,113 endothelial cells were identified, accounting for 11.05% of the total cells. Among these, 812 cells originated from normal samples, while 4,395, 992, 376, and 1,538 endothelial cells were associated with *MAP3K3*-mutated CCMs, *PIK3CA*-mutated CCMs, germline *KRIT1*-mutated CCMs, and *MAP3K3* and *PIK3CA* double-mutated CCMs, respectively (Fig. 3F). To elucidate molecular pathways, we conducted gene set enrichment analysis (GSEA) on endothelial cells from different mutation groups and control tissues (Fig. 3G and H and Supplementary Fig. 4B to E). Gene Ontology Biological Processes (GO-BP) analysis identified significant upregulation of pathways related to hypoxia response, regulation of angiogenesis, vascular development, cell adhesion, and oxygen-level responses in endothelial cells from CCM lesions compared to controls (Fig. 3G). Notably, endothelial cells from lesions harboring *MAP3K3* and *PIK3CA* double mutations exhibited enhanced activation of pathways related to vascular development and angiogenesis compared to those with only *PIK3CA* mutations (Fig. 3H). This finding suggests that *MAP3K3* mutations synergize with *PIK3CA* mutations to amplify angiogenesis-related pathways, highlighting distinct molecular mechanisms underlying CCM pathogenesis. FeaturePlot visualization of the angiogenesis pathway from WikiPathways further revealed significant upregulation in endothelial cell populations from CCM lesions (Fig. 3I), particularly in samples with *MAP3K3* mutations (Fig. 3J). These results underscore the substantial activation of angiogenic pathways in endothelial cells from CCM lesions, with *MAP3K3* mutant samples showing especially pronounced enrichment.

To further confirm the expression of pro-angiogenic factors in CCMs, we performed immunostaining for VEGFA and the endothelial cell marker CD31 in surgical specimens from CM patients with various mutations. The results showed that endothelial cells from patients harboring *MAP3K3* mutations exhibited elevated VEGFA expression compared to those from normal temporal lobe vessels. Furthermore, lesions with combined *MAP3K3* and *PIK3CA* mutations displayed significantly higher VEGFA levels than those with *PIK3CA* mutations alone. (Fig. 3K and L).

To delineate the cooperative mechanism of MAP3K3 GOF and PIK3CA GOF, we conducted bulk RNA sequencing on endothelial cells from the brains of *Map3k3*$^{\mathrm{iECGOF}}$, *Pik3ca*$^{\mathrm{iECGOF}}$, *Map3k3*$^{\mathrm{iECGOF}}$; *Pik3ca*$^{\mathrm{iECGOF}}$, and wild type littermate control mice. The mice were administered 4-OHT at P1 and harvested at P6. We enriched brain CD45-CD31+ endothelial cells using a magnetic-activated cell sorting (MACS) system for RNA sequencing (Fig. 4A). GO-BP and KEGG analyses revealed an enrichment of genes involved in the positive regulation of cell migration, angiogenesis, vascular development, and leukocyte migration in endothelial cells with *Map3k3*$^{\mathrm{iECGOF}}$ compared to wild type controls. There was also significant upregulation of genes related to extracellular matrix (ECM) receptor interactions, the PI3K-AKT signaling pathway, and the TNF signaling pathway. In contrast, endothelial cells with *Pik3ca*^{iECGOF} showed enrichment in genes associated with chromosome segregation, DNA replication, and the cell cycle compared to wild type controls (Fig. 4B). We compared the brain endothelial cells of *Map3k3*^{iECGOF}; *Pik3ca*^{iECGOF} with those of *Pik3ca*^{iECGOF}. Notably, we observed significant upregulation in pathways related to endothelial proliferation, TGF-β signaling, cytokine-cytokine receptor interactions, and the PI3K-AKT signaling pathway (Fig. 4B).

To further validate our findings in human endothelial cells, we performed bulk RNA sequencing on HUVECs infected with lentivirus encoding either human *MAP3K3*^{I441M} mutations (referred to as *MAP3K3*-MT), human *PIK3CA*^{H1047R} mutations (referred to as *PIK3CA*-MT), or an empty vector as a control. KEGG analysis of the bulk RNA sequencing data revealed significant upregulation of pathways including MAPK signaling, cytokine-cytokine receptor interaction, PI3K-AKT signaling, and TNF signaling in *MAP3K3*-MT compared to wild type controls. In contrast, *PIK3CA*-MT showed significant upregulation of genes associated with the cell cycle (Fig. 4C). These results suggest that MAP3K3 GOF in endothelial cells activates angiogenesis-related pathways, while PIK3CA GOF predominantly activates cell cycle and growth-related pathways. Together, MAP3K3 GOF enhances angiogenesis, while *PIK3CA* GOF promotes cell cycles of endothelial cells. Their combined effects synergistically amplify endothelial remodeling and angiogenesis pathways in CCMs.

MAP3K3 GOF activates VEGF

To further investigate how MAP3K3 GOF activates angiogenesis pathways and enhances the effects of PIK3CA GOF in driving CCMs, we focused on key pro-angiogenic factors VEGFA and VEGFC and quantified their expression in HUVECs using Q-PCR. Q-PCR analysis revealed significant upregulation of *VEGFA* and *VEGFC* in *MAP3K3*-MT compared to controls (*MAP3K3*-CTRL). In contrast, PIK3CA GOF had a more modest effect on the expression of *VEGFA* and *VEGFC* (Fig. 4D). Then the protein expression of VEGFA in HUVECs was detected by Western Blot. The results showed that the relative expression of VEGFA protein in *MAP3K3*-MT was significantly higher than that in the control group. However, the relative expression of VEGFA protein was decreased in *PIK3CA*-MT compared with the control group (*PIK3CA*-CTRL) (Fig. 4E). These findings suggest that MAP3K3 GOF, but not PIK3CA GOF, upregulates the expression of VEGFA in endothelial cells. VEGF interacts with its receptors on endothelial cells, initiating a signaling cascade that activates the PI3K pathway, particularly the PI3Kα isoform, and catalyzes the conversion of phosphatidylinositol-4,5-bisphosphate (PIP2) into phosphatidylinositol-3,4,5-trisphosphate (PIP3).[29] This conversion leads to the activation of downstream signaling molecules like AKT, which play crucial roles in cell survival, migration, proliferation and promotes various cellular processes essential for angiogenesis.[30, 31] The findings indicate that MAP3K3 GOF upregulates pro-angiogenic factors, including VEGFA, thereby further amplifying PI3K pathway activation in endothelial angiogenesis.

Adult-onset secondary MAP3K3 GOF drives CCMs from pre-existing DVAs

DVAs have been proposed as potential precursors to CCMs and may originate from somatic *PIK3CA* mutations.[8, 10, 13, 15, 32-36] To investigate the role of PIK3CA activation in this process, we crossed *Slco1c1*(BAC)-CreERT2 mice (Supplementary Fig.5) with R26-*Pik3ca*$^{\mathrm{H1047R}}$ mice and administered 4-OHT at P1 to induce brain endothelium-specific expression of the *Pik3ca*$^{\mathrm{H1047R}}$ mutation (*Pik3ca*$^{\mathrm{iBECGOF}}$) (Fig. 5A). MRI performed six weeks post-induction revealed dilated, low-signal vessels resembling human DVAs, and only limited CCM lesions were detected in *Pik3ca*$^{\mathrm{iBECGOF}}$ mice (Fig. 5B). We hypothesized that in adult setting, MAP3K3 GOF may function as a second hit to promote DVAs associated CCM formation. To test this hypothesis, we further injected the *Pik3ca*$^{\mathrm{iBECGOF}}$ mice with AAV-BR1-*MAP3K3*$^{\mathrm{I441M}}$ (or AAV-BR1-*MAP3K3*$^{\mathrm{WT}}$ or AAV-BR1-GFP) via the orbital veins to introduce *MAP3K3*$^{\mathrm{I441M}}$ mutation (or overexpress *MAP3K3*$^{\mathrm{WT}}$ or GFP) in brain endothelial cells (Fig. 5C). The mice were sacrificed 14 days post-injection for analysis. Visual inspection and micro-CT analysis revealed a significant increase in lesion burden in mice injected with AAV-BR1-*MAP3K3*$^{\mathrm{I441M}}$ compared to those injected with AAV-BR1-GFP (Fig. 5D-F). H&E staining of brain sections showed that *Pik3ca*$^{\mathrm{iBECGOF}}$ mice injected with either AAV-BR1-*MAP3K3*$^{\mathrm{I441M}}$ or AAV-BR1-*MAP3K3*$^{\mathrm{WT}}$ developed extensive, dilated vascular lesions (Fig. 5G). Mice receiving AAV-BR1-*MAP3K3*$^{\mathrm{WT}}$ also exhibited elevated lesion burdens, albeit to a lesser extent (Fig. 5D-G). Hemosiderin deposition can be observed around the vascular lesions (Supplementary Fig.2B). Immunofluorescence analysis demonstrated increased levels of P-S6 in the endothelial cells lining the vascular lesions of *Pik3ca*$^{\mathrm{iBECGOF}}$ mice injected with AAV-BR1-*MAP3K3*$^{\mathrm{I441M}}$, indicating activation of PI3K downstream pathways and enhanced CCM lesion formation (Fig. 5H and I). Additionally, injection of AAV-BR1-*MAP3K3*$^{\mathrm{I441M}}$ led to increased VEGFA expression in the vascular lining and peri-vascular areas

(Fig. 5J and K). These findings suggest that MAP3K3 GOF can synergize with PIK3CA GOF to exacerbate CCMs by enhancing angiogenesis and vascular remodeling in mature brains.

Increased VEGF expression switches pre-existing DVAs to CCMs

We then investigated if the subsequent acquisition of pro-angiogenic factors is the mechanism transforming pre-existing DVAs into CCMs in mature brains. We crossed *Slco1c1*(BAC)-CreERT2 mice with R26-*Pik3ca*^{H1047R} mice, administering 4-OHT at P1 to induce brain endothelium-specific expression of the *Pik3ca*^{H1047R} mutation (*Pik3ca*^{iBECGOF}). To overexpress VEGF, these mice were injected with AAV-BR1-VEGFA (or AAV-BR1-GFP as control) via the orbital veins at six weeks old age. We harvested brain tissues on day 6 as *Pik3ca*^{iBECGOF} injected with AAV-BR1-VEGFA died on day 7 post injection (Fig. 6A and B). We also injected AAV-BR1-VEGFA into age-matched wild type C57BL/6J mice. Visual inspection and micro-CT analysis revealed a significant increase in lesion burden in *Pik3ca*^{iBECGOF} mice injected with AAV-BR1-VEGFA compared to those injected with AAV-BR1-GFP. In contrast, C57BL/6J wild type mice injected with AAV-BR1-VEGFA showed no evidence of vascular lesions by day 6 postinjection (Fig. 6C-E). H&E staining of brain sections from *Pik3ca*^{iBECGOF} mice injected with AAV-BR1-VEGFA revealed extensive dilated vascular lesions in both white and gray matter (Fig. 6F). Immunofluorescence analysis demonstrated elevated levels of P-S6 in the endothelial cells lining the vascular lesions of *Pik3ca*^{iBECGOF} mice injected with AAV-BR1-VEGFA, indicating hyperactivation of the PI3K pathway (Fig. 6G and H). Immunofluorescence analysis also demonstrated higher expression of VEGFA in the vascular lining and peri-vascular areas of *Pik3ca*^{iBECGOF} mice injected with AAV-BR1-VEGFA (Fig. 6I and J). Our findings demonstrate that MAP3K3 GOF synergizes with PIK3CA GOF to drive CCM formation by activating angiogenic pathways. Specifically, MAP3K3 GOF upregulates VEGFA, which subsequently activates downstream VEGF-PI3K signaling. Notably, even in the absence of MAP3K3 GOF, overexpression of pro-angiogenic factors such as VEGFA secondary to PIK3CA GOF can trigger an angiogenic switch, promoting the progression of DVAs into CCMs. These findings position the MAP3K3-VEGF-PI3K axis as a compelling therapeutic target for preventing CCM formation.

PI3K alpha inhibitor prevents formation of CCMs

Alpelisib, a PIK3CA inhibitor, has shown therapeutic potential in conditions associated with PIK3CA-related overgrowth syndrome (PROS) by disrupting the PI3K signaling axis and has been demonstrated efficacy in treating severe *PIK3CA*-related lymphatic anomalies in both pediatric and adult patients.[37, 38] We assessed the efficacy of alpelisib in inhibiting CCMs formation in our mouse model. Similar to the previous protocol, *Map3k3*$^{\mathrm{iECGOF}}$; *Pik3cai*$^{\mathrm{ECGOF}}$ mice were given a single intraperitoneal dose of 60 μg 4-OHT at P5. Mice were subsequently treated with either vehicle or alpelisib at P7, P9, and P11, with CCM lesions assessed at P12 (Fig. 7A). Visual inspection revealed that alpelisib administration nearly completely halted CCM growth. Micro-CT analysis showed that alpelisib significantly reduced lesion formation compared to the vehicle group (Fig. 7B-D, and Supplementary Fig. 6). H&E staining indicated that alpelisib-treated mice developed only a few small venous anomalies, in contrast to the extensive lesions observed in the vehicle-treated mice (Fig. 7E). Compared to the vehicle group, no hemosiderin deposition was observed in the alpelisib-treated mice (Supplementary Fig. 2C). Immunostaining for CD31 and P-S6 in brain sections confirmed effective inhibition of the PI3K pathway in the brain endothelial cells of alpelisib-treated mice (Fig. 7F and G). We next assessed the translational potential of alpelisib using patient-derived CCM organoids established from freshly resected surgical specimens. DNA extracted from the same lesion used for primary organoid culture underwent whole-exome sequencing (300× mean coverage), which identified a *MAP3K3* p.I441M mutation (allele frequency 16.7%) and a *PIK3CA* p.E542K mutation (allele frequency 4.9%), confirming a double-mutation genotype (Supplementary Fig. 7). Treatment with alpelisib effectively suppressed PI3K pathway activity, as evidenced by a marked reduction in P-S6 expression. In parallel, alpelisib significantly increased the expression of the tight junction protein Claudin-5 compared to the vehicle control group. (Fig. 7H-M). These findings underscore alpelisib as a promising therapeutic agent for CCM disease, capable of effectively blocking the synergistic effects of the MAPK and PI3Kα pathways (Fig. 7N).

Discussion

Our study provides compelling evidence that *MAP3K3* and *PIK3CA* mutations cooperate to drive the formation and progression of CCMs through converging effects on endothelial cell behavior and vascular architecture. Using a multifaceted approach that integrates genetically engineered mouse models, single-cell and bulk transcriptomic profiling, human tissue validation, and pharmacological intervention, we demonstrate that dual activation of MAPK and PI3K signaling synergistically promotes lesion burden and angiogenic dysregulation in the central nervous system. These findings not only deepen our understanding of the molecular underpinnings of CCM pathogenesis but also offer mechanistic support for targeting the PI3Kα signaling axis in CCM patients. Our results suggest that PI3Kα inhibitors may hold therapeutic promise beyond cancer, potentially offering a precision medicine strategy for vascular malformations with defined genetic alterations.

Recent studies report that true human *CCM1* lesions exhibit reduced EC numbers, reflecting vessel pruning and chronic remodeling.[39] Our human and mouse data together clarify the nature of MAP3K3–PIK3CA synergy in CCMs. Although *PIK3CA* and *MAP3K3* GOF mutations can promote endothelial activation, neither single nor combined mutations induce overt endothelial hyperproliferation, but rather a pathological angiogenic remodeling. In mouse double-mutant ECs (*Map3k3*$^{\mathrm{iECGOF}}$; *Pik3ca*$^{\mathrm{iECGOF}}$), scRNA-seq reveals activation of vascular development, endothelial–mural communication, and ECM pathways, without large increases in EC number, confirming that synergy manifests through functional remodeling rather than proliferation.

Our findings are in line with previous studies that have implicated the RAS-MAPK pathway in promoting angiogenesis in various vascular diseases and tumors.[40-42] Notably, *MAP3K3* mutations in endothelial cells enhance the endothelial angiogenesis capacity, which, in conjunction with the activation of the PI3K pathway, results in enhanced vascular remodeling characteristic of CCMs. *PIK3CA* GOF mutations, on the other hand, primarily activate the PI3K pathway by increasing the activity of the p110α subunit, which leads to the activation of downstream signaling cascades critical for endothelial cell survival and proliferation. While the PI3K pathway plays a crucial role in vascular development, our data reveal that the combined activation of the PI3K and MAPK pathways synergistically accelerates lesion progression by intensifying angiogenesis.

The identification of VEGFA as a key downstream mediator of MAP3K3 GOF provides a novel perspective on how *MAP3K3* mutations influence angiogenic signaling. While VEGFA is widely recognized for its role in promoting angiogenesis, the present study establishes it as a critical link between *MAP3K3* and PI3K signaling in endothelial cells. This finding suggests that the MAP3K3-VEGF-PI3K axis could be a therapeutic target in CCMs, where VEGFA-driven angiogenesis is a central mechanism driving lesion growth. The concept of the "angiogenic switch", initially described in cancer biology, is particularly relevant to our findings. In tumors, the transition from avascular to vascular phases is driven by hypoxia and the upregulation of pro-angiogenic factors like VEGF.[43-45] Similarly, in *PIK3CA* mutant DVAs, AAV-mediated VEGF overexpression mimicked this switch, triggering excessive angiogenesis and accelerating lesion progression. Our study demonstrates that *MAP3K3* amplifies angiogenic pathways through the activation of downstream signaling cascades, particularly those involved in vascular remodeling and permeability. In parallel, VEGF serves as a potent inducer of angiogenesis, driving endothelial cell activation and promoting aberrant vessel formation within DVAs, ultimately leading to the development of symptomatic CCMs.

Although both CCM and PROS involve aberrant PI3K pathway activation, their genetic and pathological contexts are distinct. PROS is driven by isolated *PIK3CA* mutations leading to somatic mosaicism and segmental overgrowth affecting multiple tissues, whereas sporadic CCMs are characterized by brain-restricted vascular malformations frequently associated with *MAP3K3* gain-of-function mutations, with or without coexisting *PIK3CA* variants. In our endothelial-specific *Map3k3*^{I441M}; *Pik3ca*^{H1047R} mouse model, the lesions exhibited the classic cavernoma morphology—thin-walled, dilated capillaries devoid of intervening parenchyma—distinct from the diffuse vascular dysplasia typical of PROS. Furthermore, single-cell transcriptomic profiling revealed endothelial–mural cell interactions consistent with CCM-like pathological angiogenesis rather than proliferative overgrowth. These findings collectively confirm that the model reflects the pathogenic mechanisms of sporadic CCMs rather than PROS-related vascular anomalies.

These findings highlight the therapeutic potential of targeting the MAPK-PI3K signaling axis in the treatment of CCMs. The PI3Kα inhibitor alpelisib effectively attenuates CCM formation and reverses the pro-angiogenic effects associated with *MAP3K3* and *PIK3CA* mutations, providing a viable therapeutic strategy for cases where surgical intervention is not feasible. The ability of alpelisib to prevent CCM phenotypes in mouse models and organoids supports its potential for clinical application. Additionally, the observed synergy between MAPK and PI3K signaling in endothelial cells suggests that combination therapies, involving PI3K inhibitors and VEGF-targeted agents, may offer a more effective approach for preventing or treating CCMs.

Despite these advances, our study has several limitations. First, while our mouse models recapitulate critical aspects of human CCM pathology and provide mechanistic insight into the early synergistic effects of MAP3K3 and PIK3CA in lesion formation, species-specific differences in endothelial signaling and immune interactions mean that extrapolation to human lesion genesis should be made cautiously. Second, our therapeutic experiments used preclinical dosing and treatment windows, and the long-term safety and efficacy of PI3Kα inhibition in patients with CCM remain unknown. Additionally, most human CCM samples analyzed are sporadic lesions in this study. Our data indicate that co-activation of MAP3K3 and PIK3CA drives a pathological angiogenic program in these cases. Given that *CCM* LOF mutations can activate MAP3K3, it is plausible that similar MAP3K3–PIK3CA–mediated mechanisms may also operate in familial or other genotypes. Nevertheless, direct evidence in these contexts is currently lacking, and further studies are required to determine whether such synergistic interactions occur across different CCM genotypes and phenotypes. Consistent with the limitations of human samples, it is important to note that surgically excised CCM lesions represent fully formed and clinically active vascular malformations, which precludes direct observation of lesion initiation or early molecular events. Clinical evidence suggests that sporadic CCMs can arise from DVAs, which often harbor *PIK3CA* mutations. Our data, together with recent studies, indicate that MAP3K3 activation may act as a second hit during the DVA-to-CCM transition.[13, 46] The endothelial-specific mouse models and AAV-mediated experiments presented here allow us to interrogate early lesion formation and capture the synergistic effects of MAP3K3 and PIK3CA, providing mechanistic insights that complement observations from human lesions. To facilitate clinical translation, prospective clinical trials are needed to evaluate the therapeutic potential of PI3Kα inhibitors in well-defined patient subgroups, alongside biomarker-guided monitoring of treatment efficacy. Furthermore, integrating spatial transcriptomics and vascular imaging may help elucidate lesion microenvironment dynamics and uncover additional therapeutic targets. Together, these steps will be essential to translate our mechanistic insights into meaningful clinical interventions for CCM patients.

Data availability

All data are available in the main text or the supplementary materials. Derived data supporting the findings of this study are available from the corresponding author on request.

Acknowledgements

We thank Capital Medical University Laboratory Animal Research Center for assistance in animal experimentation. Figures 1A, 2A and C, 3A, 4A, 5A and C, 6A and B and 7A and H were created in BioRender. Hong, t. (2026) https://BioRender.com/bk4nmhk.

Funding

This work was supported by the National Natural Science Foundation of China (82425020, 82220108010, 82330038, 82471325, 82201439, 82201440), Chinese Institutes for Medical Research, Beijing (CX25YZ04), Beijing Municipal Education Commission (BPHR20220113), Beijing Physician Scientist Training Project (BJPSTP-2024-26), and Capital's Funds for Health

Improvement and Research (2022-2Z-20110), Beijing Natural Science Foundation-Haidian Original Innovation Joint Fund Project (L242030).

Competing interests

The authors report no competing interests.

Supplementary material

Supplementary material is available at *Brain* online.

References

1. Li D, Sheppard SE, March ME, et al. Genomic profiling informs diagnoses and treatment in vascular anomalies. *Nat Med*. Jun 2023;29(6):1530-1539. doi:10.1038/s41591-023-02364-x

2. Smith ER. Cavernous Malformations of the Central Nervous System. *N Engl J Med*. Mar 14 2024;390(11):1022-1028. doi:10.1056/NEJMra2305116

3. Snellings DA, Hong CC, Ren AA, et al. Cerebral Cavernous Malformation: From Mechanism to Therapy. *Circulation research*. Jun 25 2021;129(1):195-215. doi:10.1161/circresaha.121.318174

4. Stapleton CJ, Barker FG, 2nd. Cranial Cavernous Malformations: Natural History and Treatment. *Stroke*. Apr 2018;49(4):1029-1035. doi:10.1161/strokeaha.117.017074

5. Shenkar R, Shi C, Rebeiz T, et al. Exceptional aggressiveness of cerebral cavernous malformation disease associated with PDCD10 mutations. *Genet Med*. Mar 2015;17(3):188-196. doi:10.1038/gim.2014.97

6. Zafar A, Quadri SA, Farooqui M, et al. Familial Cerebral Cavernous Malformations. *Stroke*. May 2019;50(5):1294-1301. doi:10.1161/strokeaha.118.022314

7. Peyre M, Miyagishima D, Bielle F, et al. Somatic PIK3CA Mutations in Sporadic Cerebral Cavernous Malformations. *N Engl J Med*. Sep 9 2021;385(11):996-1004. doi:10.1056/NEJMoa2100440

8. Ren AA, Snellings DA, Su YS, et al. PIK3CA and CCM mutations fuel cavernomas through a cancer-like mechanism. *Nature*. 2021;594(7862):271-276. doi:10.1038/s41586-021-03562-8

9. Hong T, Xiao X, Ren J, et al. Somatic MAP3K3 and PIK3CA mutations in sporadic cerebral and spinal cord cavernous malformations. *Brain*. Oct 22 2021;144(9):2648-2658. doi:10.1093/brain/awab117

10. Weng J, Yang Y, Song D, et al. Somatic MAP3K3 mutation defines a subclass of cerebral cavernous malformation. *Am J Hum Genet*. 2021;108(5):942-950. doi:10.1016/j.ajhg.2021.04.005

11. Craig EA, Stevens MV, Vaillancourt RR, Camenisch TD. MAP3Ks as central regulators of cell fate during development. *Dev Dyn*. Nov 2008;237(11):3102-14. doi:10.1002/dvdy.21750

12. Wang Y, Rozen V, Zhao Y, Wang Z. Oncogenic activation of PIK3CA in cancers: Emerging targeted therapies in precision oncology. *Genes Dis*. Mar 2025;12(2):101430. doi:10.1016/j.gendis.2024.101430

13. Snellings DA, Girard R, Lightle R, et al. Developmental venous anomalies are a genetic primer for cerebral cavernous malformations. *Nat Cardiovasc Res*. Mar 2022;1:246-252. doi:10.1038/s44161-022-00035-7

14. Cogswell PM, Pillai JJ, Lanzino G, Flemming KD. Prevalence of Developmental Venous Anomalies in Association with Sporadic Cavernous Malformations on 7T MRI. *AJNR Am J Neuroradiol*. Dec 29 2023;45(1):72-75. doi:10.3174/ajnr.A8072

15. Castillo SD, Tzouanacou E, Zaw-Thin M, et al. Somatic activating mutations in Pik3ca cause sporadic venous malformations in mice and humans. *Sci Transl Med*. Mar 30 2016;8(332):332ra43. doi:10.1126/scitranslmed.aad9982

16. Ren J, Huang Y, Ren Y, et al. Somatic variants of MAP3K3 are sufficient to cause cerebral and spinal cord cavernous malformations. *Brain*. Sep 1 2023;146(9):3634-3647. doi:10.1093/brain/awad104

17. Tang AT, Choi JP, Kotzin JJ, et al. Endothelial TLR4 and the microbiome drive cerebral cavernous malformations. *Nature*. 2017;545(7654):305-310. doi:10.1038/nature22075

18. Lai CC, Nelsen B, Frias-Anaya E, et al. Neuroinflammation Plays a Critical Role in Cerebral Cavernous Malformation Disease. *Circulation research*. 2022;131(11):909-925. doi:10.1161/CIRCRESAHA.122.321129

19. Polster SP, Sharma A, Tanes C, et al. Permissive microbiome characterizes human subjects with a neurovascular disease cavernous angioma. *Nat Commun*. May 27 2020;11(1):2659. doi:10.1038/s41467-020-16436-w

20. Frias-Anaya E, Gallego-Gutierrez H, Gongol B, et al. Mild Hypoxia Accelerates Cerebral Cavernous Malformation Disease Through CX3CR1-CX3CL1 Signaling. *Arterioscler Thromb Vasc Biol*. Jun 2024;44(6):1246-1264. doi:10.1161/atvbaha.123.320367

21. Moshe DL, Baghaie L, Leroy F, Skapinker E, Szewczuk MR. Metamorphic Effect of Angiogenic Switch in Tumor Development: Conundrum of Tumor Angiogenesis Toward Progression and Metastatic Potential. *Biomedicines*. Jul 29 2023;11(8)doi:10.3390/biomedicines11082142

22. Guelfi S, Hodivala-Dilke K, Bergers G. Targeting the tumour vasculature: from vessel destruction to promotion. *Nat Rev Cancer*. Oct 2024;24(10):655-675. doi:10.1038/s41568-024-00736-0

23. Maiuri F, Cappabianca P, Gangemi M, et al. Clinical progression and familial occurrence of cerebral cavernous angiomas: the role of angiogenic and growth factors. *Neurosurg Focus*. Jul 15 2006;21(1):e3. doi:10.3171/foc.2006.21.1.4

24. DiStefano PV, Glading AJ. VEGF signalling enhances lesion burden in KRIT1 deficient mice. *J Cell Mol Med*. Jan 2020;24(1):632-639. doi:10.1111/jcmm.14773

25. Girard R, Zeineddine HA, Orsbon C, et al. Micro-computed tomography in murine models of cerebral cavernous malformations as a paradigm for brain disease. *J Neurosci Methods*. Sep 15 2016;271:14-24. doi:10.1016/j.jneumeth.2016.06.021

26. Yang X, Wu ST, Gao R, et al. Release of STK24/25 suppression on MEKK3 signaling in endothelial cells confers cerebral cavernous malformation. *JCI Insight*. Mar 8 2023;8(5)doi:10.1172/jci.insight.160372

27. Dao L, You Z, Lu L, et al. Modeling blood-brain barrier formation and cerebral cavernous malformations in human PSC-derived organoids. *Cell Stem Cell*. Jun 6 2024;31(6):818-833.e11. doi:10.1016/j.stem.2024.04.019

28. Ren J, Xiao X, Li R, et al. Single-cell sequencing reveals that endothelial cells, EndMT cells and mural cells contribute to the pathogenesis of cavernous malformations. *Exp Mol Med*. Mar 2023;55(3):628-642. doi:10.1038/s12276-023-00962-w

29. Graupera M, Guillermet-Guibert J, Foukas LC, et al. Angiogenesis selectively requires the p110alpha isoform of PI3K to control endothelial cell migration. *Nature*. May 29 2008;453(7195):662-6. doi:10.1038/nature06892

30. Ruan GX, Kazlauskas A. VEGF-A engages at least three tyrosine kinases to activate PI3K/Akt. *Cell Cycle*. Jun 1 2012;11(11):2047-8. doi:10.4161/cc.20535

31. Zeng L, Xiao Q, Chen M, et al. Vascular endothelial cell growth-activated XBP1 splicing in endothelial cells is crucial for angiogenesis. *Circulation*. Apr 23 2013;127(16):1712-22. doi:10.1161/circulationaha.112.001337

32. Huo R, Yang Y, Sun Y, et al. Endothelial hyperactivation of mutant MAP3K3 induces cerebral cavernous malformation enhanced by PIK3CA GOF mutation. *Angiogenesis*. May 2023;26(2):295-312. doi:10.1007/s10456-023-09866-9

33. Ren J, Wang D, Wang L, et al. Clinical, genomic, and histopathologic diversity in cerebral cavernous malformations. *Acta Neuropathol Commun*. Feb 5 2025;13(1):23. doi:10.1186/s40478-025-01940-1

34. Zhang J, Abou-Fadel J, Renteria M, et al. Cerebral cavernous malformations do not fall in the spectrum of PIK3CA-related overgrowth. *J Neurol Neurosurg Psychiatry*. Apr 27 2022;doi:10.1136/jnnp-2022-328901

35. Zhang J, Croft J, Le A. Familial CCM Genes Might Not Be Main Drivers for Pathogenesis of Sporadic CCMs-Genetic Similarity between Cancers and Vascular Malformations. *J Pers Med*. Apr 17 2023;13(4)doi:10.3390/jpm13040673

36. Limaye N, Kangas J, Mendola A, et al. Somatic Activating PIK3CA Mutations Cause Venous Malformation. *Am J Hum Genet*. Dec 3 2015;97(6):914-21. doi:10.1016/j.ajhg.2015.11.011

37. Venot Q, Blanc T, Rabia SH, et al. Targeted therapy in patients with PIK3CA-related overgrowth syndrome. *Nature*. Jun 2018;558(7711):540-546. doi:10.1038/s41586-018-0217-9

38. Delestre F, Venot Q, Bayard C, et al. Alpelisib administration reduced lymphatic malformations in a mouse model and in patients. *Sci Transl Med*. Oct 6 2021;13(614):eabg0809. doi:10.1126/scitranslmed.abg0809

39. Han Z, Lei C, Zhou Z, Liu Y, Zhao Y, He S. Single-cell transcriptome profiling reveals dynamic cell populations and immune infiltration in cerebral cavernous malformation. *Front Immunol*. 2025;16:1592343. doi:10.3389/fimmu.2025.1592343

40. Murillo MM, Zelenay S, Nye E, et al. RAS interaction with PI3K p110α is required for tumor-induced angiogenesis. *J Clin Invest*. Aug 2014;124(8):3601-11. doi:10.1172/jci74134

41. Yuan S, Stewart KS, Yang Y, et al. Ras drives malignancy through stem cell crosstalk with the microenvironment. *Nature*. Dec 2022;612(7940):555-563. doi:10.1038/s41586-022-05475-6

42. Nikolaev SI, Vetiska S, Bonilla X, et al. Somatic Activating KRAS Mutations in Arteriovenous Malformations of the Brain. *N Engl J Med*. Jan 18 2018;378(3):250-261. doi:10.1056/NEJMoa1709449

43. Bergers G, Benjamin LE. Tumorigenesis and the angiogenic switch. *Nat Rev Cancer*. Jun 2003;3(6):401-10. doi:10.1038/nrc1093

44. Dor Y, Porat R, Keshet E. Vascular endothelial growth factor and vascular adjustments to perturbations in oxygen homeostasis. *Am J Physiol Cell Physiol*. Jun 2001;280(6):C1367-74. doi:10.1152/ajpcell.2001.280.6.C1367

45. De Palma M, Hanahan D. Milestones in tumor vascularization and its therapeutic targeting. *Nat Cancer*. Jun 2024;5(6):827-843. doi:10.1038/s43018-024-00780-7

46. Ren J, Hong T, Zhang H. Angioarchitecture and genetic variants of spinal cord cavernous malformations and associated developmental venous anomalies: a case report. *Childs Nerv Syst*. Jul 2023;39(7):1945-1948. doi:10.1007/s00381-023-05887-3

Figure legends

Figure 1 *Map3k3*$^{\mathbf{I441M}}$ and *Pik3ca*$^{\mathbf{H1047R}}$ synergized during cavernous malformation formation in the neonatal mice. (**A**) *Cdh5* (PAC)–CreERT2 mice were bred with R26-*Map3k3*^{I441M} mice; R26-*Pik3ca*^{H1047R} mice, or R26-*Map3k3*^{I441M}; *Pik3ca*^{H1047R} mice separately to inducibly drive the endothelium-specific expression of *Map3k3*^{I441M}; *Pik3ca*^{H1047R} mutation and double mutations. (**B**) Schematic showing neonatal induction of *Map3k3*^{I441M} and/or *Pik3ca*^{H1047R} expression. Injection of 4-OHT at P1 was used to inducibly drive expression of indicated mutation. Brains were harvested at P6. (**C**) Representative visual (top panel) and paired micro-CT (bottom panel) images of littermate control, *Map3k3*^{iECGOF}, *Pik3ca*^{iECGOF}, and *Map3k3*^{iECGOF}; *Pik3ca*^{iECGOF} mice at P6. (**D**) Micro-CT quantification of lesion volumes (top panel) and lesion volumes normalized to total brain volume (bottom panel) of indicated genotype at P6. Littermate control, *n*=6; *Map3k3*^{iECGOF}, *n*=7; *Pik3ca*^{iECGOF}, *n*=6; *Map3k3*^{iECGOF}; *Pik3ca*^{iECGOF}, *n*=7. (**E**) Representative images of H&E stained histological sections of *Map3k3*^{iECGOF}, *Pik3ca*^{iECGOF}, and *Map3k3*^{iECGOF}; *Pik3ca*^{iECGOF} mice brain section. Left panel showed CCM lesion location in the cerebral cortex, and right panel showed CCM lesion location in the cerebellum. Arrowheads indicate vascular lesions. *Map3k3*^{iECGOF} developed scattered small vascular lesions in both hindbrain and forebrain, while *Pik3ca*^{iECGOF} mice developed small vascular lesions mostly in hindbrain. *Map3k3*^{iECGOF}; *Pik3ca*^{iECGOF} mice developed multiple small vascular lesions throughout the hindbrain and forebrain. In low magnification images (top row), scale bar=200 μm and in high magnification images of the boxed area (bottom row), scale bars=50 μm. (**F**) Immunofluorescence staining for P-S6 and endothelial cell marker CD31 of littermate control, *Map3k3*^{iECGOF}, *Pik3ca*^{iECGOF}, and *Map3k3*^{iECGOF}; *Pik3ca*^{iECGOF} mice hindbrain section. Representative images are shown. White arrowheads indicate non-endothelial P-S6 positive cells, and yellow arrowheads indicate P-S6 positive endothelial cells. Scale bars, 20 μm. (**G**) Quantitative analysis of immunofluorescence staining for P-S6/CD31 in littermate control, *Map3k3*^{iECGOF}, *Pik3ca*^{iECGOF}, and *Map3k3*^{iECGOF}; *Pik3ca*^{iECGOF} mice hindbrain section was shown. Data were obtained from 6 fields of view from each of 3 mice. (**H**) Immunofluorescence staining for P-S6 on CCM samples sections of patients carried with different mutations. Representative images are shown. Scale bars, 20 μm. (**I**) Quantitative analysis of immunofluorescence staining for P-S6/CD31 in CCM samples sections of patients carried with different mutations. Data were obtained from 6-7 fields of view from each of 3 CCM patients. Data are presented as mean ± SD (D, G, E). Statistical significance between groups was determined by one-way ANOVA. *$P < 0.05$, **$P < 0.01$, ***$P < 0.001$, ****$P < 0.0001$, and ns, not significant.

Figure 2 ScRNA-seq of mouse CCM models reveals activation of pro-angiogenic pathways in endothelial cells.

(A) Pups were injected with 4-OHT and harvested at specified time points to generate *Map3k3*^{iECGOF}, *Pik3ca*^{iECGOF} mice (double mutations mice) and littermate control. **(B)** Visual appearance of the brains of *Map3k3*^{iECGOF}, *Pik3ca*^{iECGOF} mice and littermate control mice. (**C**) Schematic workflow of scRNA-seq analysis. Transcriptomic profiles were generated from 4 mice cerebellum, including 2 CCM lesions with double mutations and 2 littermate control tissues, using 10× Genomics sequencing. **(D)** Violin plots represent the distribution of detected genes, counts, and percentage of mitochondrial RNAs, respectively. (**E**) UMAP plot of 53,164 high-quality single cells from double mutations lesions and littermate control. (**F**) Marker-based cell-type annotation identified 11 distinct cell types across all samples: neurons, neuron precursors, oligodendrocytes, neural stem cells, microglia, endothelial cells, oligodendrocyte precursors (OPC), astrocytes, ependymal cells, pericytes, and fibroblasts. (**G**) UMAP plot displaying the clustering of the eleven cell types across 53,164 single cells. (**H**) Proportion of the eleven cell types in double mutations lesions and littermate control. (**I**) Proportion of double mutations lesions and littermate control in the eleven cell types. (**J**) UMAP plot highlighting endothelial cell and mural cells subclusters in double mutations lesions and littermate control, which re-clustered into 3 endothelial cells subcluster, pericytes, and fibroblasts. (**K**) UMAP plot highlighting endothelial cell clusters in control and CCM samples. A total of 847 endothelial cells were identified, with 311 from control samples and 536 cells associated with *Map3k3* and *Pik3ca* double-mutated CMs. (**L**) Proportion of the endothelial cells and mural cells subtypes in double mutations lesions and littermate control. (**M**) GO-BP analysis of endothelial cells subgroup 1 revealed significant upregulation of pathways related to regulation of angiogenesis, vascular development, collagen metabolic process, and macrophage migration in double mutations lesions compared to littermate controls. (**N**) GO-BP analysis of pericytes from lesions with *Map3k3* and *Pik3ca* double mutations showed pathways changes related to endothelial development, differentiation and adhesion compared to littermate control.

Figure 3 ScRNA-seq of human CCM lesions reveals synergistic effects of *MAP3K3* and *PIK3CA* mutations on angiogenesis. (**A**) Schematic workflow of scRNA-seq analysis. Transcriptomic profiles were generated from 12 human samples, including 9 CCM lesions and 3 control normal brain tissues, using 10× Genomics sequencing. (**B**) UMAP plot of 73,434 high-quality single cells from control and CCM samples, highlighting transcriptional heterogeneity within CCM lesions. The 9 CCM lesions were grouped based on the following mutations: 2 with *MAP3K3* mutations, 4 with *PIK3CA* mutations, 2 with *MAP3K3* and *PIK3CA* double mutations, and 1 with germline *KRIT1* mutations (K654Sfs*21). (**C**) Marker-based cell-type annotation identified nine distinct cell types across all samples: astrocytes, B cells, endothelial cells, macrophages, microglia, mural cells, neurons, oligodendrocytes, and T cells. (**D**) Proportion of the nine cell types in control samples and CCM lesions. (**E**) UMAP plot displaying the clustering of the nine cell types across 73,434 single cells from control and CCM samples. (**F**) UMAP plot highlighting endothelial cell clusters in control and CCM samples across different genotypes. A total of 8,113 endothelial cells were identified, with 812 from control samples and 4,395, 992, 376, and 1,538 cells associated with *MAP3K3*-mutated CCMs, *PIK3CA*-mutated CCMs, germline *KRIT1*-mutated CCMs, and *MAP3K3* and *PIK3CA* double-mutated CCMs, respectively.(**G**) GO-BP analysis of endothelial cells revealed significant upregulation of pathways related to hypoxia response, regulation of angiogenesis, vascular development, cell adhesion, and oxygen-level responses in CCM lesions compared to controls. (**H**) GO-BP analysis of endothelial cells from lesions with *MAP3K3* and *PIK3CA* double mutations showed enhanced activation of pathways related to vascular development and angiogenesis compared to lesions with only *PIK3CA* mutations. (**I**) FeaturePlot visualization of the angiogenesis pathway (WikiPathways) demonstrated significant upregulation in endothelial cell populations from CCM lesions compared to controls. (**J**) FeaturePlot visualization of the angiogenesis pathway within endothelial cells from lesions harboring *MAP3K3* mutants, *PIK3CA* mutants, and *MAP3K3* & *PIK3CA* double mutants. Notably, lesions with *MAP3K3* mutations exhibited significant upregulation of angiogenesis pathways. (**K**) Immunostaining for VEGFA and CD31 in CCM samples carrying different mutations. Representative images are shown. Scale bars, 20 μm. (**L**) Quantitative analysis of immunofluorescence staining for VEGFA/CD31 in CCM samples harboring different mutations was shown. Data were obtained from 6-8 fields of view from each of 3 CCM patients. Data are presented as mean ± SD (L). Statistical significance between groups was determined by one-way ANOVA. *$P < 0.05$, **$P < 0.01$, ***$P < 0.001$, ****$P < 0.0001$, and ns, not significant.

Figure 4 *MAP3K3*$^{\text{I441M}}$ activates pro-angiogenic pathways and *PIK3CA*$^{\text{H1047R}}$ activates cell cycle progression. (**A**) Scheme of mice brain endothelial cells enrichment with MACS system. Mice brains were harvested at P6 and brain ECs were enriched by depletion of CD45-positive cells using CD45 MicroBeads and followed by selection of CD31-positive cells using CD31 MicroBeads. Then the collected brain ECs were processed for RNA-seq. Littermate control, *n*=3; *Map3k3*$^{\text{iECGOF}}$, *n*=2; *Pik3ca*$^{\text{iECGOF}}$, *n*=3; *Map3k3*$^{\text{iECGOF}}$; *Pik3ca*$^{\text{iECGOF}}$, *n*=3. (**B**) GO-BP (represented by red bars) and KEGG analyses (represented by blue bars) from the RNA-seq data of the indicated groups are shown (padj<0.01, FDR corrected). (**C**) KEGG analyses from the RNA-seq data of the HUVECs infected with lentivirus encoding human *MAP3K3*$^{\text{I441M}}$

mutations, human *PIK3CA*^{H1047R} mutations, or an empty vector as a control are shown (padj<0.01, FDR corrected). (**D**) Q-PCR analysis of *VEGFA* and *VEGFC* in HUVECs infected with lentivirus-*MAP3K3*^{I441M} and *PIK3CA*$^{H1047R.}$ *VEGFA* and *VEGFC* expression levels were normalized to *GAPDH* and presented as fold changes relative to the control. Data are presented as mean ± SD from three independent experiments. (**E**) Representative Western blot image and quantitative analysis of VEGFA expression in HUVECs infected with lentivirus-*MAP3K3*^{I441M} and lentivirus-*PIK3CA*^{H1047R}. GAPDH was used as a loading control. Data are presented as mean ± SD from three independent experiments. Statistical significance between groups was determined by unpaired Student's two-tailed t-test (D, E). **P* < 0.05, ***P* < 0.01, ****P* < 0.001, *****P* < 0.0001, and ns, not significant.

Figure 5 Adult-onset secondary MAP3K3 GOF drive CCMs from pre-existing DVAs. (**A**) *Slco1c1* (BAC)-CreERT2 mice were bred with R26-*Pik3ca*^{H1047R} mice to inducibly drive the brain endothelium-specific expression of *Pik3ca*^{H1047R} mutations. (**B**) 4-OHT was injected to *Pik3ca*^{iBECGOF} at P1 to inducibly drive expression of *Pik3ca*^{H1047R} at neonatal stage. MRI performed six weeks post-induction revealed dilated, low-signal vessels resembling human DVAs, and limited CCM lesions were detected in *Pik3ca*^{iBECGOF} mice. *n*=2. Yellow arrowheads indicate DVAs. Blue arrowheads indicate CCM lesion. (**C**) 4-OHT was injected to *Pik3ca*^{iBECGOF} at P1 to inducibly drive expression of *Pik3ca*^{H1047R} at neonatal stage, followed by injection of AAV-BR1-*MAP3K3*^{I441M} (or AAV-BR1-*MAP3K3*^{WT}, or AAV-BR1-GFP) through orbital veins at 6 weeks to drive an additional *MAP3K3*^{I441M} mutation (or overexpression of *MAP3K3*^{WT}, or GFP) in the brain ECs. Mice were harvested at AAV post-injections 14 days. (**D**) Representative visual and paired micro-CT images of *Pik3ca*^{iBECGOF} injected with different AAV. (**E**) Micro-CT quantification of lesion volumes of *Pik3ca*^{iBECGOF} injected with different AAV. AAV-GFP, *n*=6; AAV-*MAP3K3*^{WT}, *n*=6; AAV-*MAP3K3*^{I441M}, *n*=6. (**F**) Micro-CT quantification of lesion volumes normalized to total brain volume of *Pik3ca*^{iBECGOF} injected with different AAV. AAV-GFP, *n*=6; AAV-*MAP3K3*^{WT}, *n*=6; AAV-*MAP3K3*^{I441M}, *n*=6. (**G**) Representative images of H&E stained histological sections of cerebellum of *Pik3ca*^{iBECGOF} injected with different AAV. Scale bars, 50 µm. (**H**) Immunostaining for P-S6 and endothelial cell marker CD31 of *Pik3ca*^{iBECGOF} injected with different AAV mice hindbrain section. Scale bars, 20 µm. (**I**) Quantitative analysis of immunofluorescence staining for P-S6/CD31 in *Pik3ca*^{iBECGOF} injected with different AAV mice hindbrain section was shown. Data were obtained from 6-7 fields of view from each of 3 mice. (**J**) Immunostaining for VEGFA and endothelial cell marker CD31 of *Pik3ca*^{iBECGOF} injected with different AAV mice hindbrain section. Scale bars, 20 µm. (**K**) Quantitative analysis of immunofluorescence staining for VEGFA in *Pik3ca*^{iBECGOF} injected with different AAV mice hindbrain section was shown. Data were obtained from 7-9 fields of view from each of 3 mice. Data are presented as mean ± SD (D, E, H, J). Statistical significance between groups was determined by one-way ANOVA. *$P < 0.05$, **$P < 0.01$, ***$P < 0.001$, ****$P < 0.0001$, and ns, not significant.

Figure 6 Increased VEGF expression switches CCMs from Pre-existing DVAs. (**A**) *Slco1c1* (BAC)-CreERT2 mice were bred with R26-*Pik3ca*^{H1047R} mice to inducibly drive the brain endothelium-specific expression of *Pik3ca*^{H1047R} mutation. (**B**) 4-OHT was injected to *Pik3ca*^{iBECGOF} at P1 to inducibly drive expression of *Pik3ca*^{H1047R} in brain ECs at neonatal stage, followed by injection of AAV-BR1-VEGFA through orbital veins at 6 weeks to drive overexpression of VEGFA in the brain ECs. Mice were harvested at AAV post-injections 6 days. (**C**) Representative visual and paired micro-CT images of *Pik3ca*^{iBECGOF} injected with AAV-BR1-GFP or AAV-BR1-VEGFA. Wild type mice were also injected of AAV-BR1-VEGFA through orbital veins at 6 weeks and harvested at AAV post-injections 6 days. (**D**) Micro-CT quantification of lesion volumes of wild type mice injected with AAV-BR1-VEGFA, *Pik3ca*^{iBECGOF} injected with AAV-BR1-GFP or AAV-BR1-VEGFA. Wild type+AAV-BR1-VEGFA, *n*=7; *Pik3ca*^{iBECGOF}+AAV-GFP; *n*=6; *Pik3ca*^{iBECGOF}+AAV-BR1-VEGFA, *n*=5. (**E**) Micro-CT quantification of lesion volumes normalized to total brain volume of wild type mice C57BL/6J injected with AAV-BR1-VEGFA, *Pik3ca*^{iBECGOF} injected with AAV-BR1-GFP or AAV-BR1-VEGFA. Wild type+AAV-BR1-VEGFA, *n*=7; *Pik3ca*^{iBECGOF}+AAV-GFP; *n*=6; *Pik3ca*^{iBECGOF}+AAV-BR1-VEGFA, *n*=5. (**F**) Representative images of H&E stained histological sections of cerebellum of Wild type C57BL/6J mice injected with AAV-BR1-VEGFA; *Pik3ca*^{iBECGOF} injected with AAV-GFP; *Pik3ca*^{iBECGOF} injected with AAV-BR1-VEGFA mice. Scale bars, 50μm. (**G**) Representative images of immunostaining for P-S6 and endothelial cell marker CD31 of Wild type C57BL/6J mice injected with AAV-BR1-VEGFA; *Pik3ca*^{iBECGOF} injected with AAV-GFP; *Pik3ca*^{iBECGOF} injected with AAV-BR1-VEGFA mice hindbrain section. Scale bars, 20 μm. (**H**) Quantitative analysis of immunofluorescence staining for P-S6/CD31 in Wild type C57BL/6J mice injected with AAV-BR1-VEGFA; *Pik3ca*^{iBECGOF} injected with AAV-GFP; *Pik3ca*^{iBECGOF} injected with AAV-BR1-VEGFA mice hindbrain section was shown. Data were obtained from 6-7 fields of view from each of 3 mice. (**I**) Representative images of immunostaining for VEGFA and endothelial cell marker CD31 of Wild type C57BL/6J injected with AAV-BR1-VEGFA; *Pik3ca*^{iBECGOF} injected with AAV-GFP; *Pik3ca*^{iBECGOF} injected with AAV-BR1-VEGFA mice hindbrain section. Scale bars, 20 μm. (**J**) Quantitative analysis of immunofluorescence staining for VEGFA in Wild type C57BL/6J mice injected with AAV-BR1-VEGFA; *Pik3ca*^{iBECGOF} injected with AAV-GFP; *Pik3ca*^{iBECGOF} injected with AAV-BR1-VEGFA mice hindbrain section was shown. Data were obtained from 6-7 fields of view from each of 3 mice. Data are presented as mean ± SD (D, E, H, J). Statistical significance between groups was determined by one-way ANOVA. *$P < 0.05$, **$P < 0.01$, ***$P < 0.001$, ****$P < 0.0001$, and ns, not significant.

Figure 7 Alpelisib prevents CCM lesion formation. (**A**) Schematic showing the protocol for alpelisib or vehicle treatment of neonatal *Map3k3*^{iECGOF}; *Pik3ca*^{iECGOF} mice. (**B**) Representative visual and paired micro-CT images of the littermates treated with either vehicle or alpelisib. (**C**) Micro-CT quantification of lesion volumes following treatment with vehicle or alpelisib. Vehicle, *n*=6; alpelisib, *n*=7. (**D**) Micro-CT quantification of lesion volumes normalized to total brain volume following treatment with vehicle or alpelisib. Vehicle, *n*=6; alpelisib, *n*=7. (**E**) Representative images of H&E stained histological sections of the littermates treated with either vehicle or alpelisib. In low magnification images, scale bar=200 μm and in high magnification images, scale bar=50 μm. (**F**) Immunostaining for P-S6 and endothelial cell marker CD31 in hindbrain sections from vehicle or alpelisib treated *Map3k3*^{iECGOF}; *Pik3ca*^{iECGOF} mice. Scale bars, 20 μm. (**G**) Immunostaining quantification of P-S6/CD31 ratio in hindbrain sections from vehicle or alpelisib treated *Map3k3*^{iECGOF}; *Pik3ca*^{iECGOF} mice was shown. Data were obtained from 6-7 fields of view from each of 3 organoids. (**H**) Schematic illustration showing the protocol for primary human CCM organoid culture and alpelisib treatment. Primary cavernoma tissues were excised, immediately immersed in Hibernate medium, and minced into several pieces. These minced tissues were then cultured individually in BBB medium for 7 days, during which they developed into spherical organoids. Subsequently, the organoids were treated with 50 μM alpelisib for an additional 7 days. Finally, the organoids were collected for frozen sectioning and immunofluorescence staining. (**I**) Representative phase-contrast microscopy image depicting the sequential development of CCM organoids from primary human CCM tissue. Scale bars, 100 μm. (**J**) Immunostaining for P-S6 and endothelial cell marker CD31 in organoids sections from vehicle or alpelisib treatment. Scale bars, 20 μm. (**K**) Quantitative analysis of immunofluorescence staining for P-S6/CD31 in primary human CCM organoids sections from vehicle or alpelisib treatment group was shown. Data were obtained from 5-7 fields of view from each of 3 organoids. (**L**) Immunostaining for Claudin-5 and endothelial cell marker CD31 in primary human CCM organoids sections from vehicle or alpelisib treatment. Scale bars, 20 μm. (**M**) Quantitative analysis of immunofluorescence staining for Claudin-5/CD31 in primary human CCM organoids sections from vehicle or alpelisib treatment group was shown. Data were obtained from 6-7 fields of view from each of 3 organoids. (**N**) Diagram showing the angiogenic switch mechanism that the initial accumulation of *PIK3CA* mutation requires additional factors, such as *MAP3K3* mutations or increased pro-angiogenic factors, to drive lesion growth. The PI3Kα inhibitor alpelisib effectively prevents CCM formation and reverses pro-angiogenic mechanisms in preclinical models with these mutations. Data are presented as mean ± SD (C, D, G, K, M). Statistical significance between groups was determined by unpaired Student's two-tailed t-test. **P < 0.01, ***P < 0.001 and ****P < 0.0001.

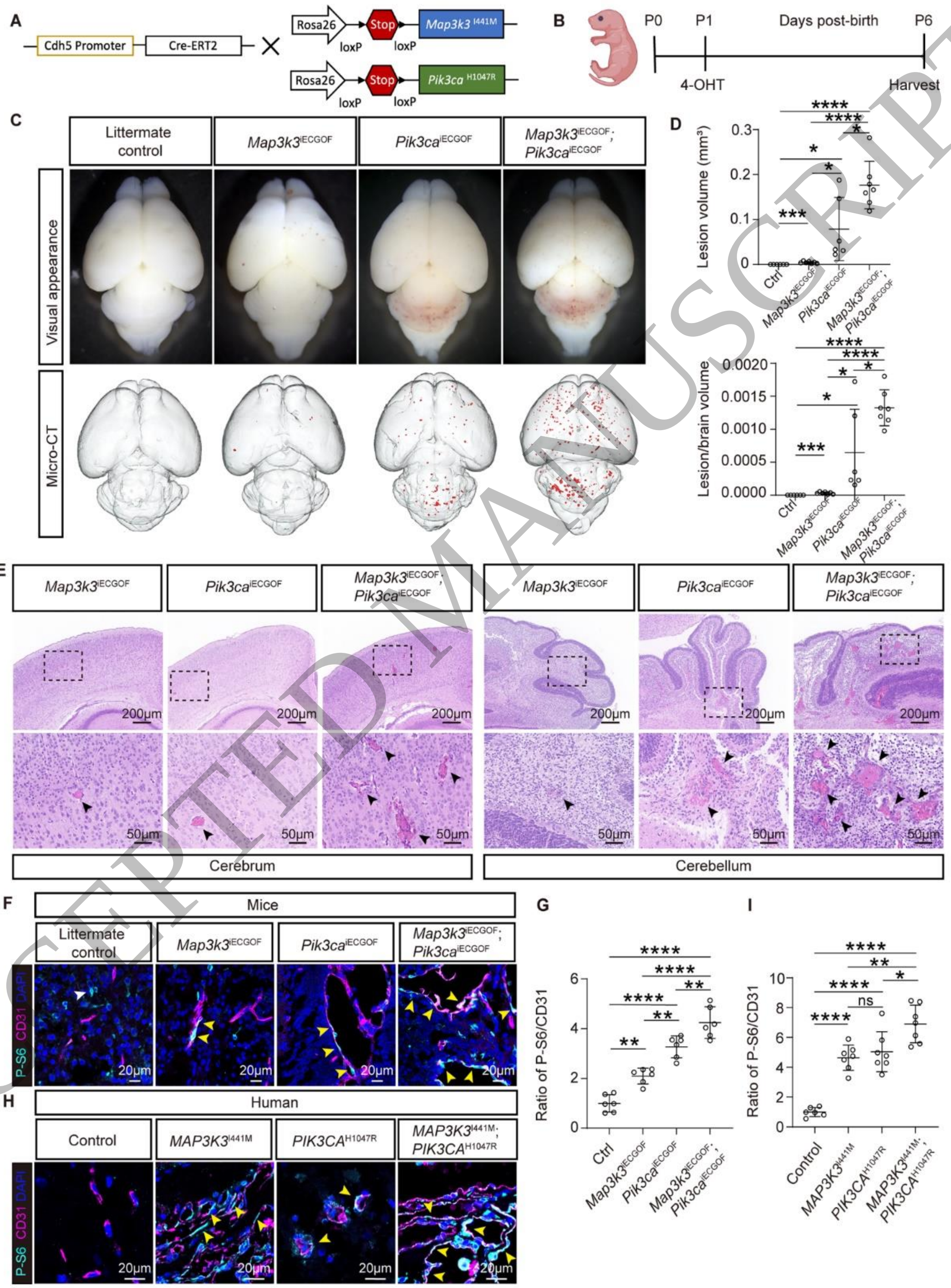

Figure 1

185x240 mm (x DPI)

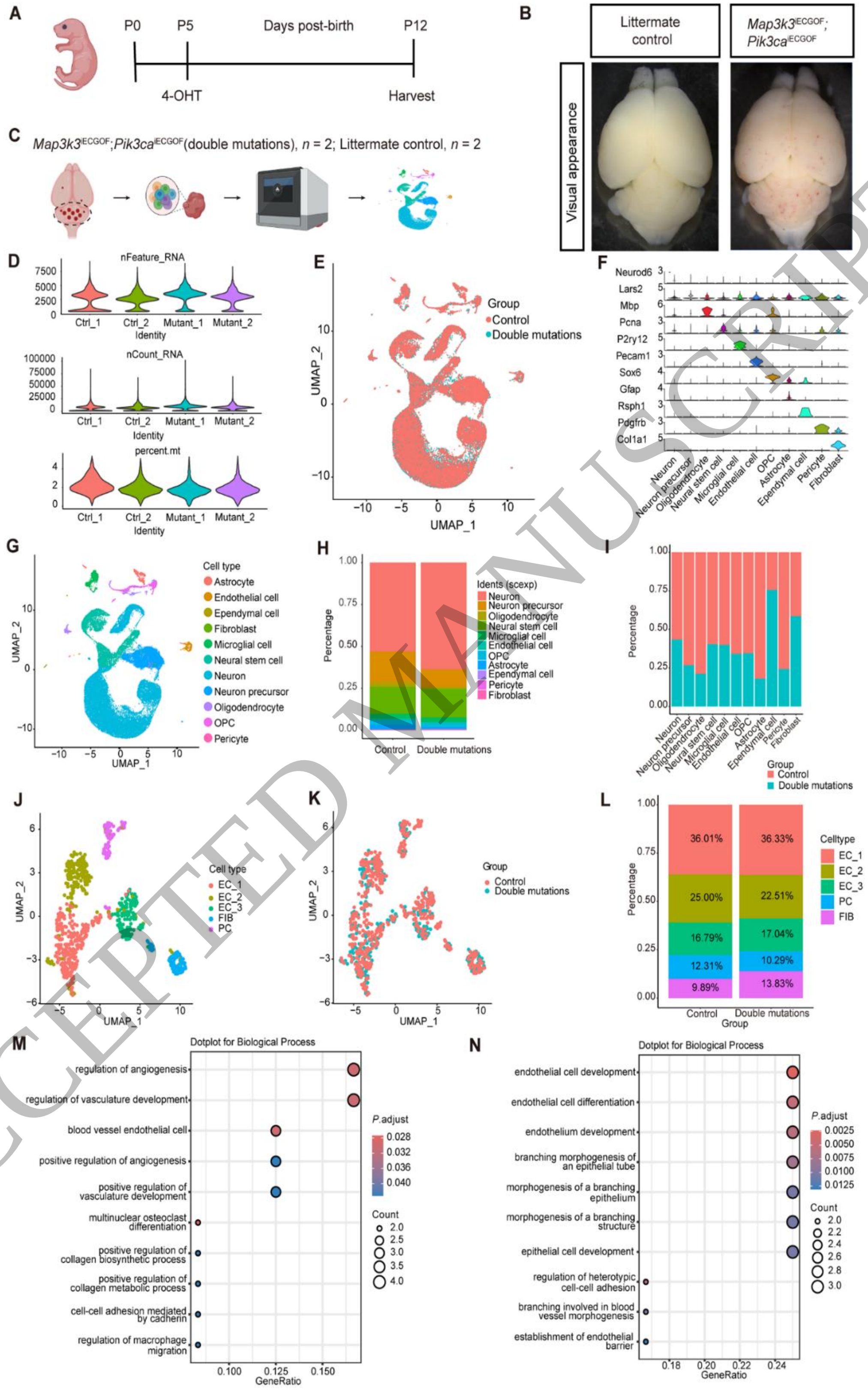

Figure 2

165x238 mm (x DPI)

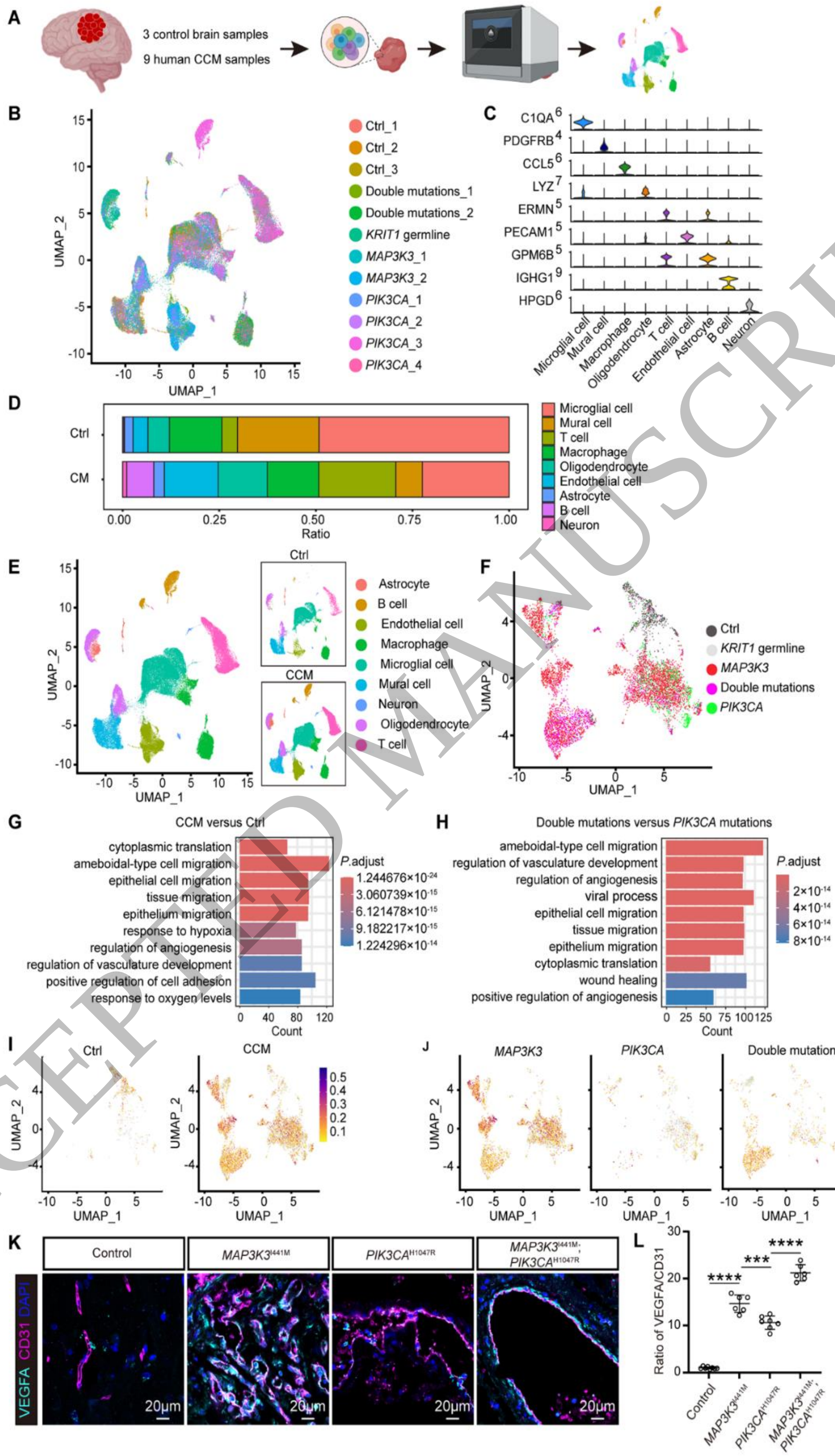

Figure 3

157x240 mm (x DPI)

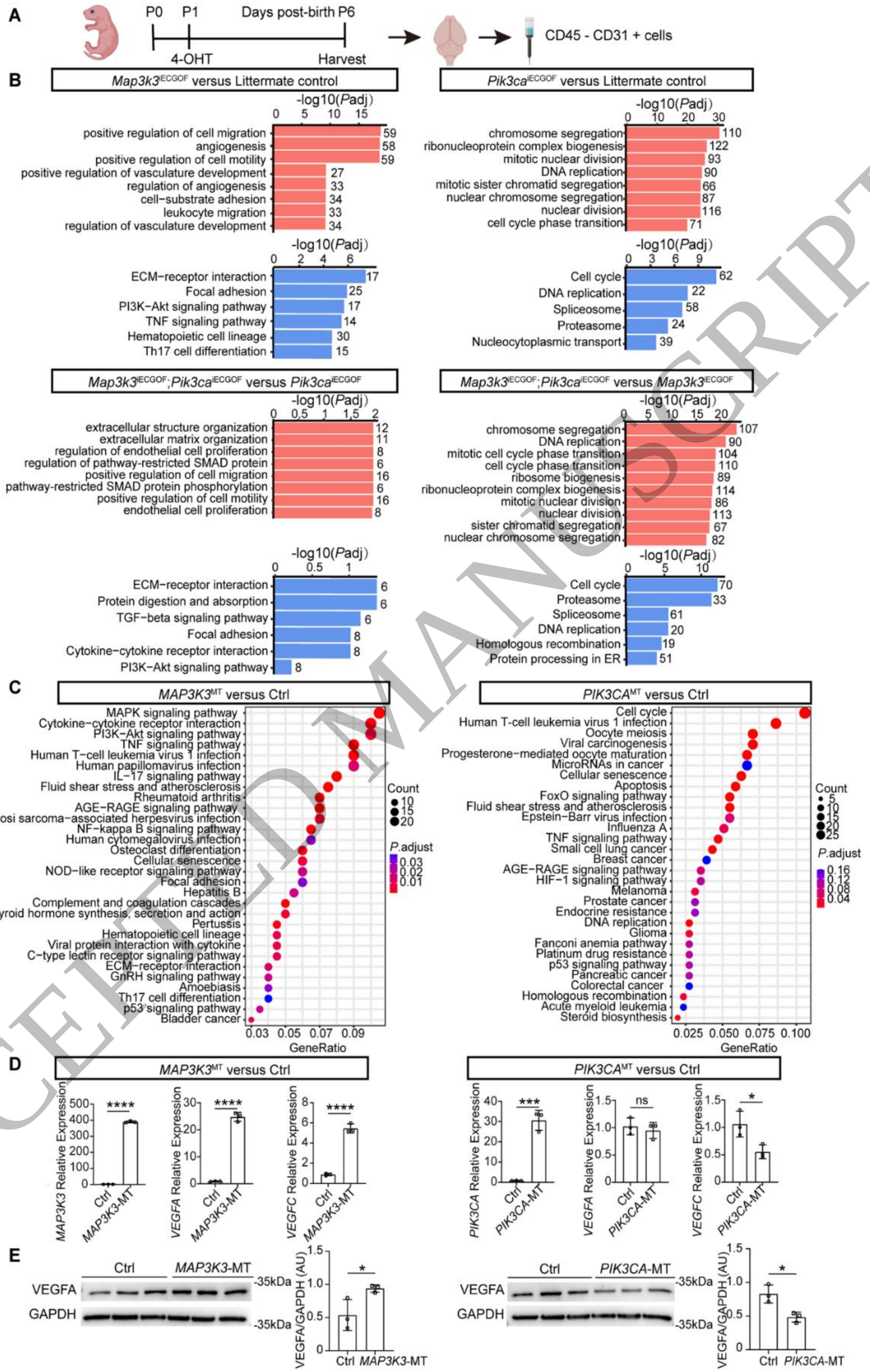

Figure 4

165x240 mm (x DPI)

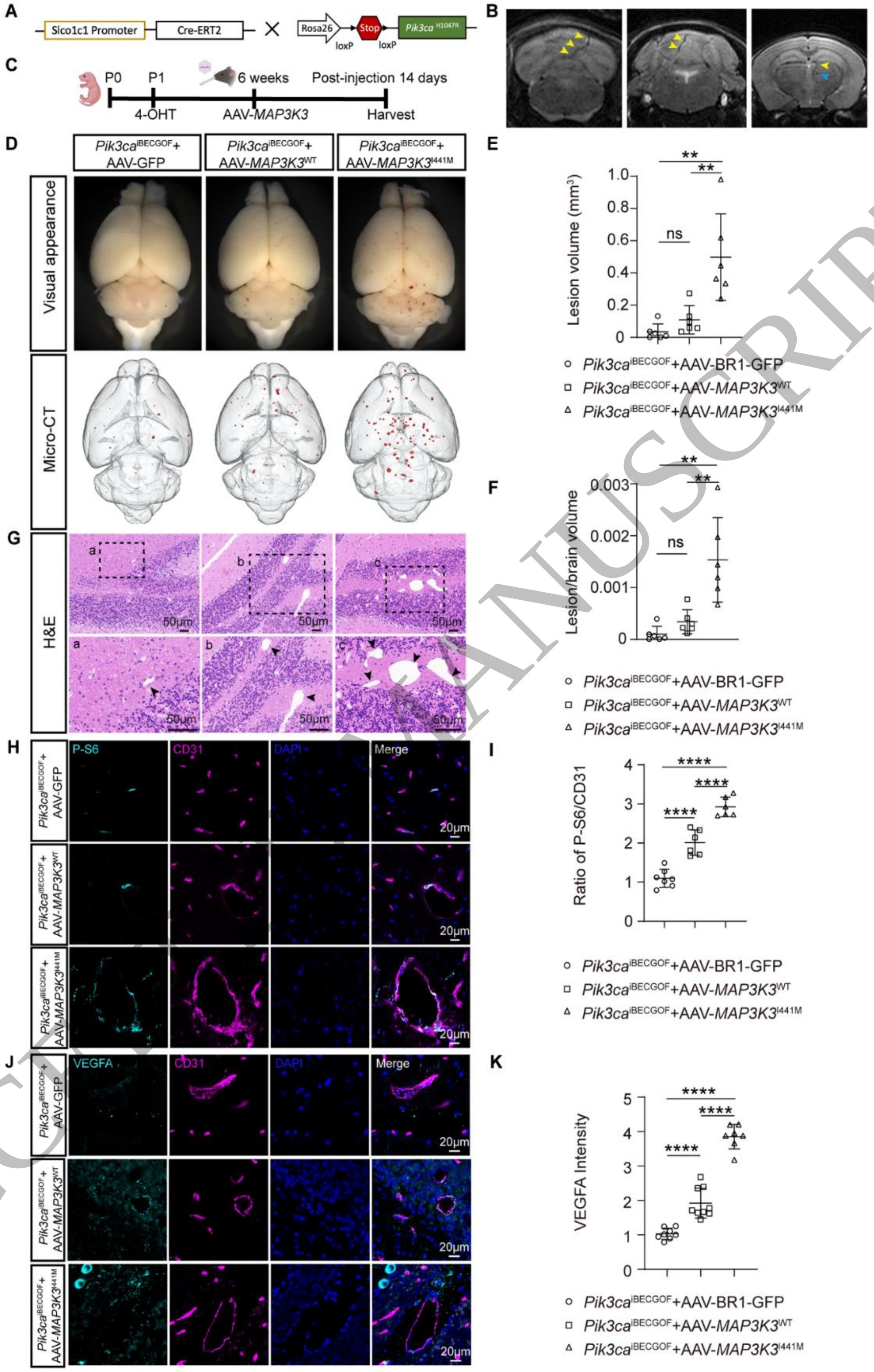

Figure 5
159x240 mm (x DPI)

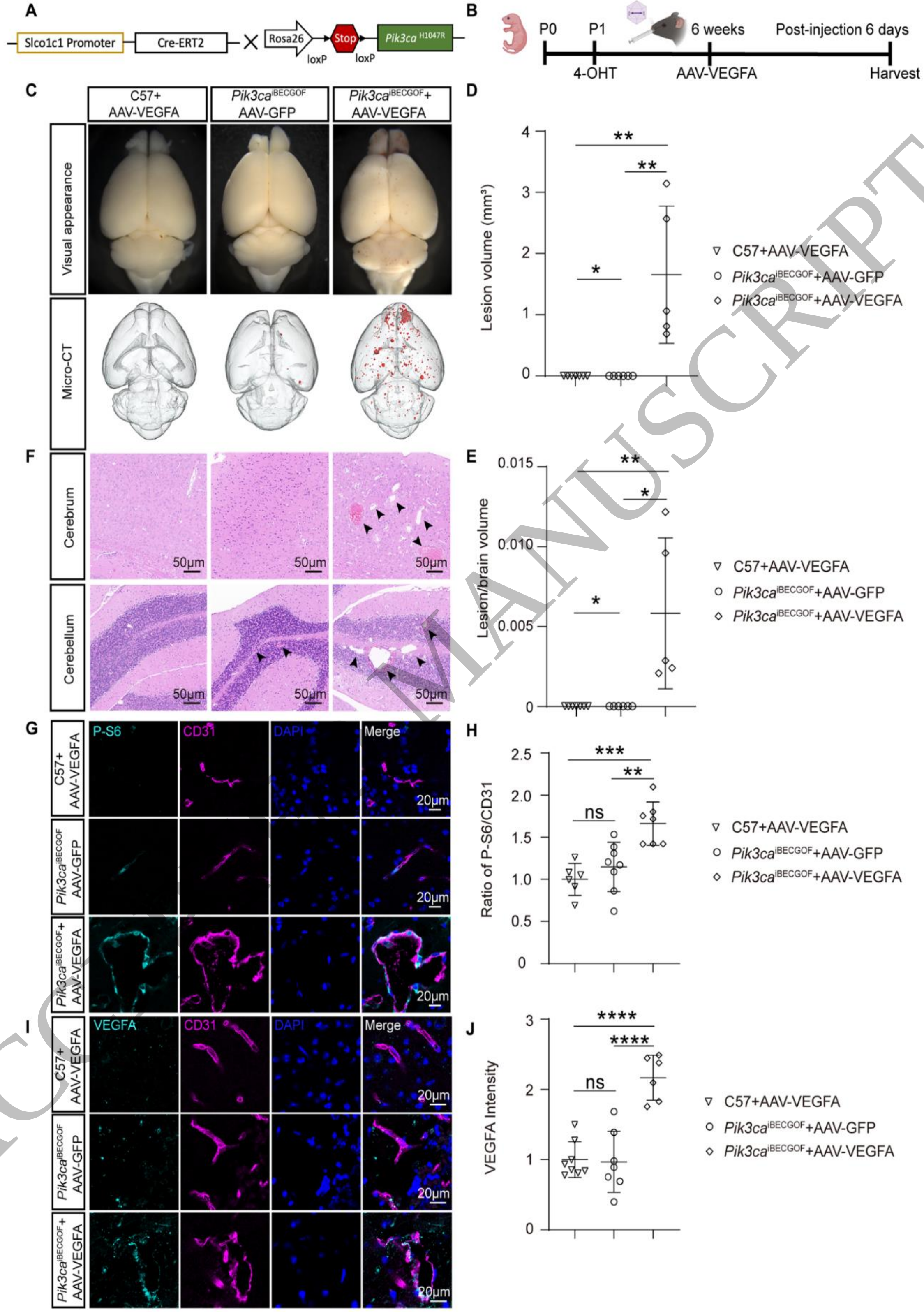

Figure 6

180x240 mm (x DPI)

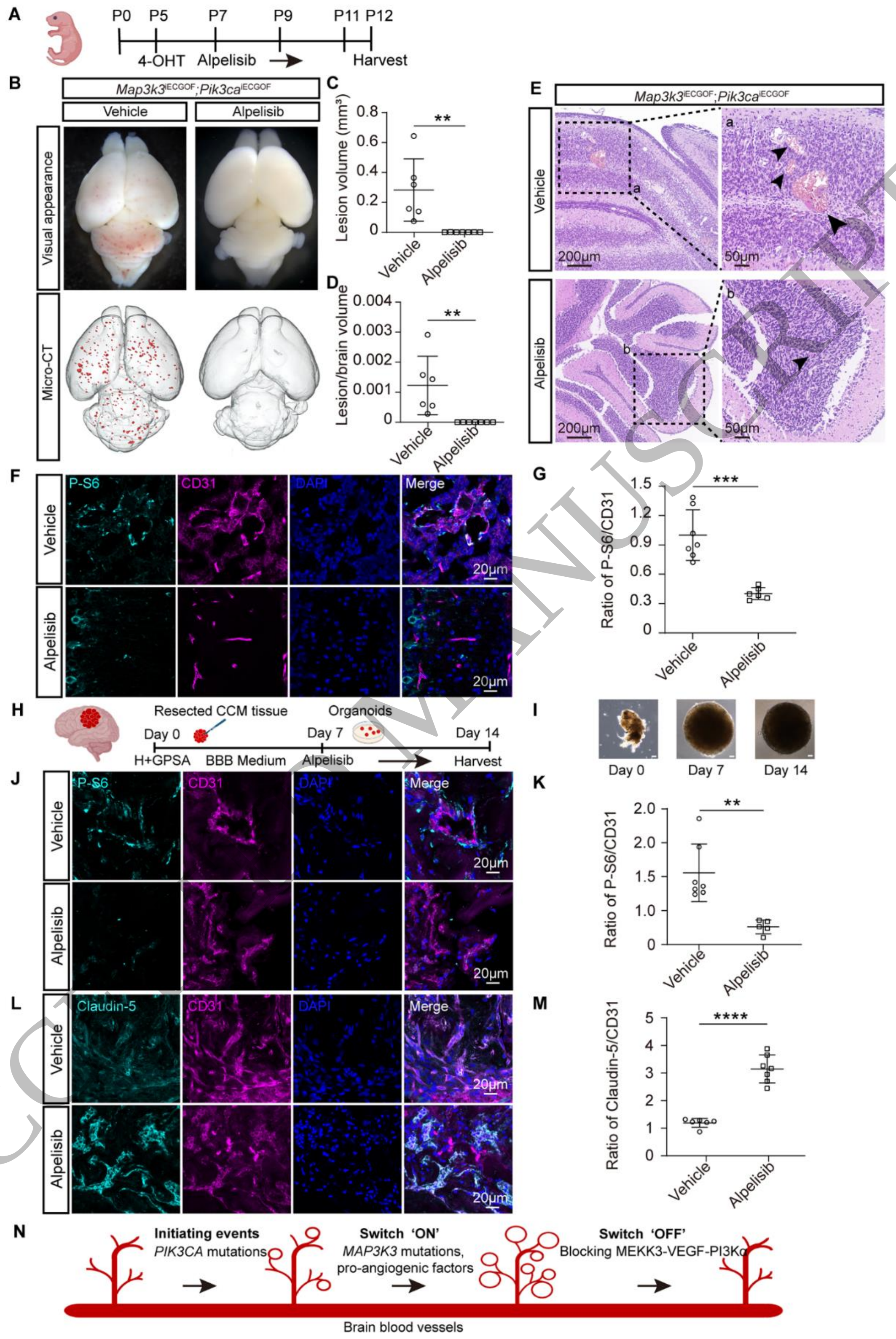

Figure 7

162x240 mm (x DPI)